Medical Image Analysis 58 (2019) 101534

Contents lists available at ScienceDirect

Medical Image Analysis

journal homepage: www.elsevier.com/locate/media

Learning the implicit strain reconstruction in ultrasound elastography using privileged information

Zhifan Gao[a], Sitong Wu[b,c], Zhi Liu[d], Jianwen Luo[d], Heye Zhang[e,*], Mingming Gong[f], Shuo Li[a,g,h,*]

[a] Department of Medical Biophysics, Western University, London N6A 3K7, Canada
[b] Shenzhen Institutes of Advanced Technology, Chinese Academy of Sciences, Shenzhen, 518055, China
[c] Shenzhen College of Advanced Technology, University of Chinese Academy of Sciences, Shenzhen, 518055, China
[d] Departmemt of Biomedical Engineering, School of Medicine, Tsinghua University, Beijing, 100084, China
[e] School of Biomedical Engineering, Sun Yat-Sen University, Shenzhen, 510006, China
[f] School of Mathematics and Statistics, The University of Melbourne, Parkville, VIC 3010, Australia
[g] Department of Medical Imaging, Western University, London N6A 3K7, Canada
[h] Digital Imaging Group of London, London N6A 3K7, Canada

ARTICLE INFO

Article history:
Received 15 January 2019
Revised 15 July 2019
Accepted 17 July 2019
Available online 19 July 2019

Keywords:
Quasi-static ultrasound elastography
Implicit model
Deep neural network
Learning using privileged information
Strain reconstruction

ABSTRACT

Quasi-static ultrasound elastography is an importance imaging technology to assess the conditions of various diseases through reconstructing the tissue strain from radio frequency data. State-of-the-art strain reconstruction techniques suffer from the inexperienced user unfriendliness, high model bias, and low effectiveness-to-efficiency ratio. The three challenges result from the explicitness characteristic (i.e. explicit formulation of the reconstruction model) in these techniques. For these challenges, we are the first to develop an *implicit* strain reconstruction framework by a deep neural network architecture. However, the classic neural network methods are unsuitable to the strain reconstruction task because they are difficult to impose any direct influence on the intermediate state of the learning process. This may lead the map learned by the neural network to be biased with the desired map. In order to correct the intermediate state of the learning process, our framework proposes the learning-using-privileged-information (LUPI) paradigm with causality in the network. It provides the causal privileged information besides the training examples to help the network learning, while makes these privileged information unavailable at the test stage. This improvement can narrow the search region of the map learned by the network, and thus prompts the network to evolve towards the actual ultrasound elastography process. Moreover, in order to ensure the causality in LUPI, our framework proposes a physically-based data generation strategy to produce the triplets of privileged information, training examples and labels. This data generation process can approximately describes the actual ultrasound elastography process by the numerical simulation based on the tissue biomechanics and ultrasound physics. It thus can build the causal relationship between the privileged information and training examples/labels. It can also address the medical data insufficiency problem. The performance of our framework has been validated on 100 simulation data, 42 phantom data and 4 real clinical data by comparing with the ground truth performed by an ultrasound simulation system and four state-of-the-art methods. The experimental results show that our framework is well agreed (average bias is 0.065 for strain reconstruction) with the ground truth, as well as superior to these state-of-the-art methods. These results can demonstrate the effectiveness of our framework in the strain reconstruction.

1. Introduction

Quasi-static ultrasound elastography is a crucial ultrasound imaging technology to indicate the conditions of diseases (e.g. inflammation, hypertrophy, edema, and fibrosis) by assessing the tissue stiffness (Zaleska-Dorobisz et al., 2014; Hoerig et al., 2017; Shiina et al., 2015). This imaging technology aims to reconstruct

* Corresponding authors.
E-mail addresses: zhangheye@mail.sysu.edu.cn (H. Zhang), slishuo@gmail.com (S. Li).

https://doi.org/10.1016/j.media.2019.101534
1361-8415/

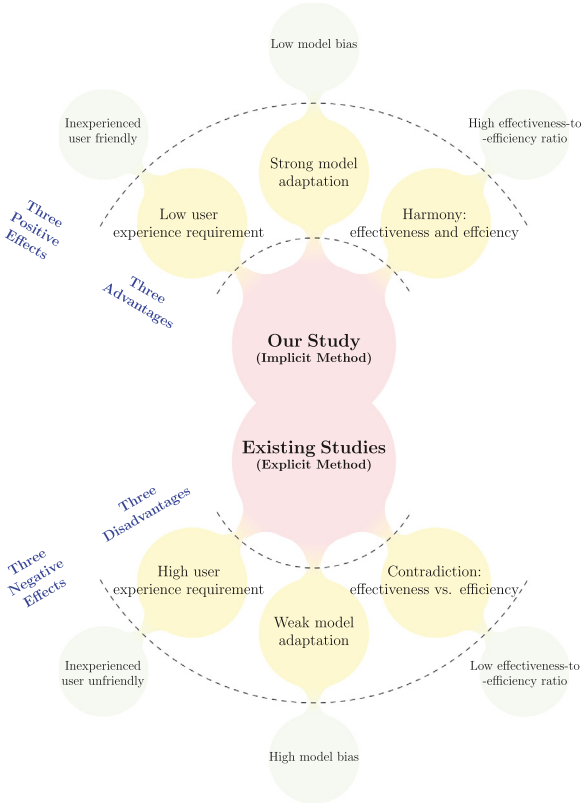

Fig. 1. Superiority of our study to the previous quasi-static ultrasound elastography technologies. The previous studies aim at the explicit strain reconstruction method, and thus bring in three disadvantages (dependency on user's experience, weak model adaptation, and effectiveness-efficiency contradiction). Our study is the first to focus on the implicit method. It can overcome the above disadvantages and bring the three benefits (inexperienced use friendly, low model bias and high effectiveness-to-efficiency ratio) to the quasi-static ultrasound elastography.

the tissue strain distribution within the suspected lesion area according to the radio frequency (RF) data before and after compressing the target tissue by means of an ultrasound transducer (Ophir et al., 1991). It thus has the ability to evaluate the tissue elasticity (indicated by the reconstructed strain) that is difficultly acquired in the commonly-used B-mode ultrasound imaging (Barr et al., 2015; Ferraioli et al., 2015; Cosgrove et al., 2017; Barr et al., 2017; Cosgrove et al., 2013). Its ability of tissue elasticity evaluation brings in the significant improvement of clinical diagnosis accuracy for many diseases (e.g. 15.5% accuracy improvement in the diagnosis of malignant lymph node (Zhang et al., 2009), because the elasticity is a significant indicator of organic diseases. European Federation of Societies for Ultrasound in Medicine and Biology (EFSUMB) have shown that the quasi-static ultrasound elastography is able to reach about 90% sensitivity and specificity in disease diagnosis of many organs, such as breast, thyroid and prostate (Bamber et al., 2013).

However, the state-of-the-art strain reconstruction techniques in quasi-static ultrasound elastography suffer from three major challenges (see Fig. 1). All these challenges result from their all use of explicit models to solve the strain reconstruction problem, i.e. the intrinsic solution formulation for strain reconstruction is explicit.

The first challenge is the weak model adaptation, i.e. a single model is difficult to adapt all RF data. It originates from the explicit characteristic of the strain reconstruction models in all existing literature (Rivaz et al., 2009, 2011; Brusseau et al., 2008; Kuzmin et al., 2015; Yuan et al., 2011; Pellot-Barakat et al., 2004). The explicitness leads that all models can obtain the strain reconstruction solution (i.e. strain field) only from some RF data, depending on their own characteristics (e.g. field smoothness (Hashemi and Rivaz, 2017) and optical flow consistency (Zakaria et al., 2010)). This implies that each explicit model occupies a separate bounded region in the solution space for the strain reconstruction problem. i.e. the solution set of all explicit models is composed of many separate regions. Hence, all explicit models may poorly perform on the RF data whose corresponding strain reconstruction solutions fall outside their solution set. This indicates the explicit models weakly adapts the various RF data, and thus may provide the strain reconstruction solution with high model bias.

The second challenge is the contradiction between the effectiveness and efficiency in the explicit methods. The effectiveness denotes the reconstruction performance of the ultrasound elastography method, and the efficiency denotes its computational cost. Although having high computational efficiency, the methods with simple formulated model are difficult to accurately reconstruct the tissue strain in noise-corrupted RF data. This is because these methods may be apt to produce the noise-induced error (e.g. peak error and jitter error) (Walker and Trahey, 1995). To reduce the noise disturbance, varieties of complex reconstruction model (e.g. biomechanical model) are developed at the cost of the computational efficiency due to the extensive iterative calculations (Lu et al., 2014). Thus, the existing explicit methods have low effectiveness-to-efficiency ratio, i.e. the ratio of the reconstruction performance to the computational cost of the ultrasound elastography method.

The final challenge is the requirement of the manual model selection when using the explicit methods. The manual model selection comes from the different advantages and disadvantages of various explicit methods. To satisfy the requirement of the specific clinical scenario, the user should select the appropriate one in various explicit methods for strain reconstruction according to data characteristics and performance requirement. Thus, the manual model selection highly relies on the user's professional experience and is unfriendly to the inexperienced user.

Classic implicit methods (i.e. the general model without explicitly modeling the process within the input-output map) are unsuitable for strain reconstruction owing to its time-consuming characteristic, although they can be naturally considered as a potential alternative to tackle the challenges in the explicit method. All these methods (e.g. variational inference (Wainwright and Jordan, 2008) and particle filtering (Fearnhead, 2002)) require numerous computations in sampling from the approximate data density during the optimization (e.g. Monte Carlo methods (Gilks et al., 1995)). The high computational requirement limits these implicit methods for strain reconstruction in clinical practice. This is the potential reason that no implicit method for strain reconstruction has appeared in the literature to our best knowledge.

Recent implicit methods based on the deep neural network have the potential to address the challenges of the explicit methods and the classic implicit methods for strain reconstruction. First, these methods can largely reduce the computation with respect to the classic methods due to no iteration calculation. Then, they are able to cope with the weak model adaptation challenge and lead to the low model bias by learning the reconstruction process from a large set of solution space. Accordingly, they can naturally address the effectiveness-efficiency contradiction challenge because of their low model bias and high computational efficiency. Finally, they are capable to tackle the manual model selection challenge as its ability to well approximate various models from its forward multilayer inference structure (Schmidhuber, 2015; Guo et al., 2016).

Nevertheless, the traditional deep neural network is unsuitable for the direct use in the strain reconstruction task. This is because it is incapable to impose any direct influence on the internal feature representation of the input that the network should focus on

during the learning process (Shi and Kim, 2017; Bisla and Choromanska, 2018). This drawback is particularly serious in the medical fields (such as ultrasound elastography) which require the complex learning models but have limited training data. Thus, the network has the potential to learn the inference model mismatching the actual map between training data and labels, because its internal feature representation may not be related to the target task (Bisla and Choromanska, 2018).

In this paper, we propose a brand-new quasi-static ultrasound elastography framework based on the deep neural network for implicit strain reconstruction, i.e. inference the map from the RF data to issue strain field (RF-to-strain map). For enabling the ability of the network to directly influence the internal feature representation, our framework applies an advanced learning paradigm named learning using privileged information (LUPI) (Vapnik and Izmailov, 2015) to the network, and is thus called UE-LUPI. The UE-LUPI provides some additional information called privileged information besides the training example to help the network learning, while makes these privileged information unavailable at the test stage (Vapnik and Vashist, 2009). It is able to narrow the search region of the map learned by the network, and thus prompts the network to evolve towards the actual ultrasound elastography process. Specifically, we consider the tissue displacement as the appropriate privileged information. According to the quasi-static ultrasound elastography (Ophir et al., 1991; Treece et al., 2011), the RF data is used to compute the tissue displacement, and the tissue displacement is used to compute the tissue strain. It brings in the causal relationship: RF data$\rightarrow$ tissue displacement $\rightarrow$ tissue strain. This causal relationship can reduce the model complexity, as well as satisfy the no-harm guarantee (i.e. not harm the learning process) in the LUPI paradigm (Lambert et al., 2018). Moreover, this causality endows the network with the ability to influence the intermediate state (i.e. displacement) in the learning process, and thus induce the network to gradually learn the actual ultrasound elastography process. However, the actual tissue displacement and strain tags can not obtained from RF data by any direct measurement technique in clinical practice. For tackling this problem, UE-LUPI proposes a strategy to generate the triplet of training data, privileged information and training labels based on the numerical simulation according to tissue biomechanics and ultrasound physics. This strategy is capable to provide reliable privileged information by building the causal relationship among training data, privileged information and training labels to approximately describe the actual ultrasound elastography process. It is motivated by the extensive use of numerical simulation in the literature of quasi-static ultrasound elastrography (e.g. (Rivaz et al., 2011; Hashemi and Rivaz, 2017)). In addition, this strategy is able to address the clinical data insufficiency issue through generating various training data and labels. It can thus overcome the model overfitting, as well as preserve all rare and precious clinical data for the model validation.

Our contributions can be summarized as follows:

1. We are the first to propose a framework (UE-LUPI) for the implicit strain reconstruction in order to improve the user friendliness, model adaptation, and effectiveness-to-efficiency ratio in the current clinical application.
2. We use the causal LUPI learning paradigm to help the network inference by correcting the intermediate state in the learning process. This strategy can prompt the RF-to-strain map learned by the network to evolve towards the actual ultrasound elastography process. Particularly, the tissue displacement is used as the causal privileged information for improving the performance of the RF-to-strain inference.
   We consider the tissue displacement as the appropriate privileged information. The causal relationship of the tissue displacement with the RF data and tissue strain can reduce the model complexity, as well as satisfy the no-harm guarantee
3. We propose a strategy based on tissue biomechanics and ultrasound physics to obtain the privileged information that is unavailable in clinical practice. This strategy can lead that the data generation process to appropriately approximate the actual ultrasound elastography process. It can ensure the causality of the privileged information (tissue displacement) with the training examples (RF data) and labels (tissue strain), and cause the network learning with the privileged information to be suitable for real scenarios. It is also capable to address the model overfitting due to data insufficiency and keep the rare clinical data for model validation.

This study has advantages over our preliminary study in MICCAI conference (Wu et al., 2018): (1) Applying the LUPI learning paradigm to the neural network for correcting the intermediate state in the network learning. The LUPI requires the additional information (called privileged information) besides the training examples and labels in the training stage. Our study has a LUPI learning paradigm by bringing in the displacement field as the privileged information to supervise the intermediate layer in the training stage, while the preliminary study applies two cascade networks, both of which have no privileged information. (2) Adding the causality among the RF data, tissue displacement and tissue strain to learn an end-to-end RF-strain map which do not require the tissue displacement in the test stage. This causality and the conditional independence between the input and output of the reconstruction model on the privileged information results in the reduction of the upper bound of the generalization error. (3) Enlarging the experimental datasets and comparing with more state-of-the-art methods for better validating the effectiveness and superiority of our framework.

2. Related work

2.1. LUPI for influencing the internal feature representation

LUPI is an advanced paradigm inspired by human experience of learning with teacher (Vapnik and Izmailov, 2015; Sharmanska et al., 2014): it is better that the teacher provide intuitive comments, comparisons, and explanations to students than simply tell them the answer (Lambert et al., 2018). Accordingly, the teacher in LUPI supplies the student with additional information (called privileged information) besides the training examples and labels only available in the training stage (Pechyony and Vapnik, 2010). The LUPI paradigm can be simply described as (Pechyony and Vapnik, 2010; Vapnik and Izmailov, 2015):

$$\begin{array}{ll} \text{given} & \{x_i, z_i, y_i\}, \quad i = 1, \ldots, N, x_i \in X, z_i \in Z, y_i \in Y \\ \text{purpose} & \text{learn } X \rightarrow Y \text{ with the small generalization error} \end{array} \tag{1}$$

where N is the number of training samples, x_i, z_i and y_i are training examples, privileged information, training labels, respectively. As a general framework, LUPI has shown its success in varieties of learning tasks (Feyereisl et al., 2014; Lapin et al., 2014; Lambert et al., 2018; Shi and Kim, 2017; Duan et al., 2014; Zheng et al., 2016). In the neural network, the privileged information in LUPI can be turned into various forms for specific tasks, for example, the statistical constraints in the autoencoders (Hjelm et al., 2019), the task feedback in the multi-task learning (Thung and Wee, 2018; Zhang and Yang, 2018), the label transformation in the deep supervision (Lee et al., 2015; Dong et al., 2018), the bounding annotation in the image classification (Sharmanska et al., 2013), the filter-based statistical structure in the texture synthesis

(Gatys et al., 2015), and the multiple inputs in the multi-view learning (Shi et al., 2018; Meng et al., 2018).

The main superiority of our LUPI paradigm is that the proposed privileged information has *causality* with the training examples and labels, in contrast to the *dependency* in the existing studies. The proposed *causal LUPI* is defined as the LUPI paradigm whose training examples, privileged information, training labels have the causal relationship, i.e. X causes Z, and Z causes Y. In our framework, the influence of the internal feature representation by privileged information can be viewed as the correlation of the intermediate state in the learning process, which is distinct from the commonly-used latent space constraint schemes (Chang et al., 2018; Engel et al., 2018). This is because the constraints aims to ameliorate the certain characteristics of the latent space, rather than provide the explicit knowledge about the intermediate state of the learned map $X \rightarrow Y$. This difference brings in the superiority of the proposed UE-LUPI that the learned map can evolve towards the actual ultrasound elastography process, because the intermediate state of model inference can be gradually corrected by the privileged information during the network optimization.

2.2. Quasi-static ultrasound elastography

Most quasi-static ultrasound elastography methods fall into two main categories: gradient-based methods and direct methods. The gradient-based methods usually firstly compute the time delay or phase shift between the pre- & post-compression RF data to estimate the tissue displacement. Then they use the spatial derivation to reconstruct the strain field (Zahiri-Azar and Salcudean, 2006; Ophir et al., 1991; Omidyeganeh et al., 2017; Yuan and Pedersen, 2015; Zhu and Hall, 2002). The direct methods reconstruct the strain directly from the RF data (Hasan et al., 2012). Varieties of methods aim to reduce the error from the noise disturbance and signal decorrelation, such as dynamic programming (Rivaz et al., 2009, 2014), least square method (Jiang and Hall, 2015; Shaswary et al., 2016), Kalman filter (Rivaz et al., 2011), and non-temporal analysis (DiBattista and Noble, 2014; Techavipoo and Varghese, 2004).

Few previous studies used the neural network or other machine learning methods in ultrasound elastography. Amidabadi et al. (2018) used support vector machine to classify peak hopping and jitter error for improving the performance of time delay estimation. Hoerig et al. (2017) modeled the force-displacement relationship in ultrasound elastography by the finite element analysis whose computational complexity and model complexity are reduced by the neural network. Kibria and Rivaz (2018) applied the neural network to compute the optical flow between RF scans for tissue displacement estimation.

The main difference of our UE-LUPI with the existing ultrasound elastography studies (including the neural-network-based methods) is that we are the first to learn the RF-to-strain map by the neural network for implicitly reconstructing the tissue strain. This leads to the superior characteristics of UE-LUPI including the improvement of user friendliness, the model adaptation, and the effectiveness-to-efficiency ratio.

3. Methodology

Our newly proposed UE-LUPI provides an implicit framework by the deep neural network to construct the tissue strain from RF data, shown in Fig. 2. UE-LUPI enables the LUPI learning paradigm in strain reconstruction by using the tissue displacement as the privileged information. This selection brings in the causal relationship of the privileged information with the training examples (i.e. the RF data) and labels (i.e. the tissue strain). It thus causes the training examples and labels have the conditional independency according to the ultrasound elstgraphy principle. As regards this causality, the privileged information is incorporated into a specially-designed loss term of the neural network for correcting the intermediate state of the learning process (detailed in Section 3.1 and Fig. 4) This strategy enables the direct guidance of the inner feature representation of the network for correcting the intermediate state in the learning process, which is superior to the classic neural network methods (i.e. without the LUPI paradigm). Thus, it can narrow the search region of the map learned by the network and enriched the feedback information. It further leads

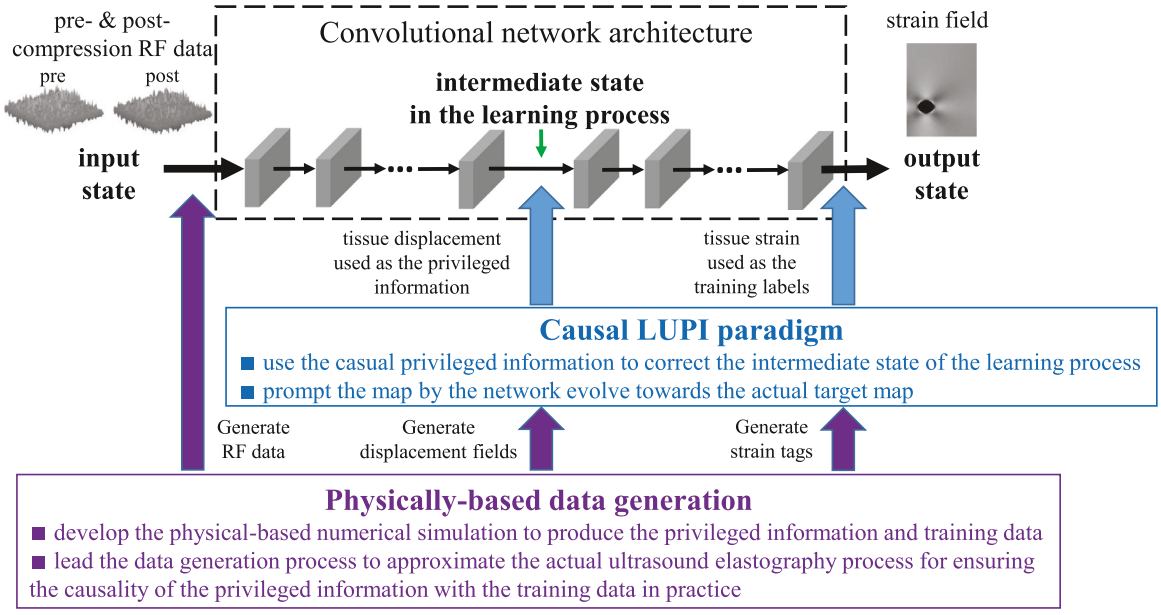

Fig. 2. Overview of UE-LUPI. UE-LUPI proposes an implicit framework based on the deep neural network to reconstruct the strain field from pre- & post-compression 2D RF data. In UE-LUPI, a causal learning-using-privileged-information (LUPI) learning paradigm is proposed to correct the intermediate state in the network learning process. Then, a physically-based data generation is proposed to produce the privileged information (tissue displacement) and training data (RF data and tissue strain) for ensuring the causality of the privileged information.

that the map learned by UE-LUPI is able to evolve towards the actual ultrasound physical process. Furthermore, for ensuring the causality of the privileged information, UE-LUPI applies the numerical simulation to produce the triplets of RF data, tissue displacement and tissue strain according to tissue biomechanics and ultrasound physics (detailed in Section 3.2 and Fig. 5). In addition, this strategy enables the training process of the neural network in the absence of clinical tissue displacement and strain tags. The above behaviors lead the effectiveness of the UE-LUPI in the strain reconstruction task.

3.1. Causal privileged information for correcting intermediate state in the network learning process

3.1.1. Formulation of the causal LUPI learning paradigm

Our UE-LUPI has the causal LUPI learning paradigm by considering tissue displacement as the privileged information, i.e. add a causal constraint in Eq. (1). It can be formulated as

$$\begin{array}{ll} \text{given} & \{x_i, z_i, y_i\}, \quad i = 1, \ldots, N, x_i \in X, z_i \in Z, y_i \in Y \\ \text{subject to} & X \to Z \to Y \ \text{ has the causal relationship} \\ \text{purpose} & \text{learn } X \to Y \ \text{ with the small generalization error} \end{array} \tag{2}$$

where N is the number of training samples, x_i, z_i and y_i are the training examples, privileged information, training labels, respectively.

The causal relationship in Eq. (2) can be formulated by the functional causal model (Goudet et al., 2018; Zhang et al., 2016):

$$S_j \leftarrow f_j(S_{Pa(k;\mathcal{G}),E_k}) \tag{3}$$

where $\mathbf{S} = \{S_1, S_2, \ldots\}$ is the set of observation variables in the causal graph $\mathcal{G}$. $S_{Pa(k;\mathcal{G})}$ is set of the direct causal variable S_j based on the causal mechanism f_j. E_1 and E_2 are the noise. In the proposed LUPI learning paradigm, the casual graph $\mathcal{G}$ is specified as the Eq. (4) and shown in Fig. 3.

$$Z = f_1(X, E_1), \quad Y = f_2(Z, E_2) \tag{4}$$

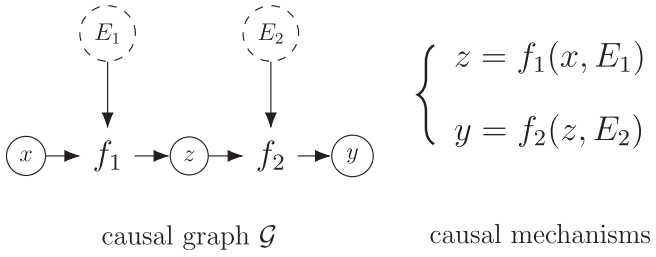

Fig. 3. The functional causal model to show the direct causal relationship in the proposed causal LUPI learning paradigm.

Thus, the purpose to learn the $X \to Y$ in Eq. (2) can be simplified to learn the two maps f_1: $X \to Z$ and f_2: $Z \to Y$.

3.1.2. Supervision-enriched neural network to solve the causal LUPI problem

In order to solve the causal LUPI problem, UE-LUPI uses the neural network to learn the functions f_1 and f_2. In particular, UE-LUPI constructs a loss term to provide the feedback information from the privileged information to the intermediate layer of the network (see Fig. 4(a)). With this loss term, the traditional loss formulation of the end-to-end neural network can be transformed into

$$loss = L(\hat{y}, y) + L(\hat{z}, z) \tag{5}$$

where x is the training examples used as the network input. $\hat{y} = f_2(f_1(x))$ is the predict value of the training labels y in the neural network. $\hat{z} = f_1(x)$ is the predict value of the privileged information z. L is the loss function. f_1 and f_2 denote the function map of $X \to Z$ and $Z \to Y$, which corresponds to the front part and back part of the network, respectively. Accordingly, the neural network in our UE-LUPI aims to learn the map $X \to Z \to Y$, while the classic neural network focuses on the map $X \to Y$. Their difference is shown in Fig. 4. Thus, the causal privileged information z is able to facilitate the neural network learning because the extra supervision information are provided.

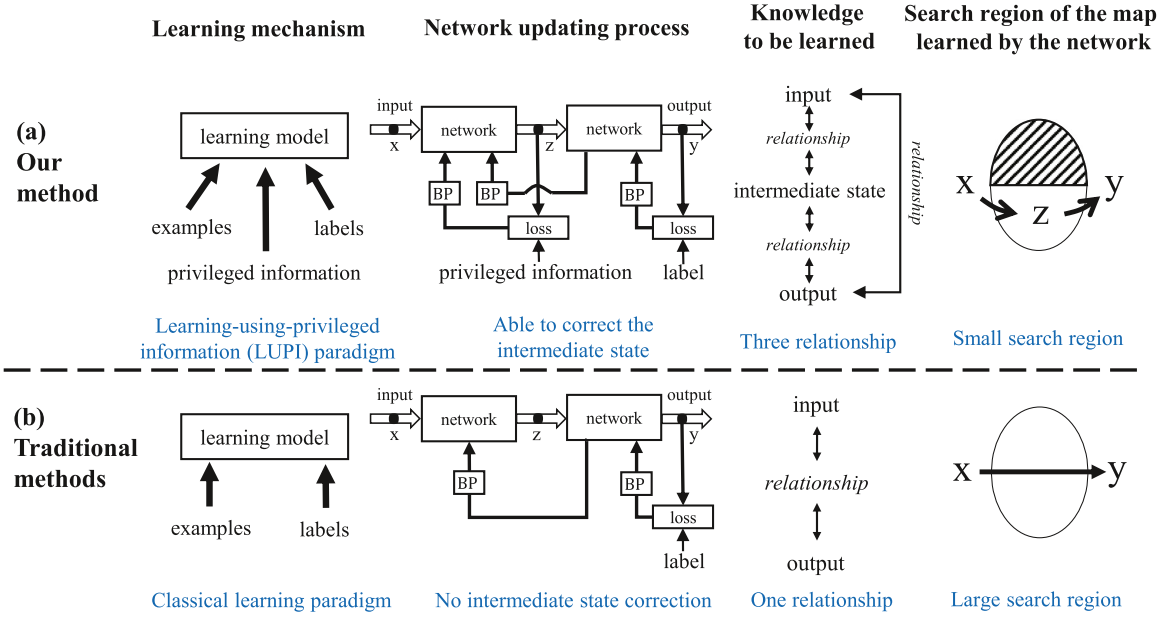

Fig. 4. Superiority of UE-LUPI to the traditional deep neural network methods. (a) Our UE-LUPI applies the learning-using-privileged-information learning paradigm. It can correct the intermediate state in the network learning process, and leads the network to learn from more knowledge. Thus, it can narrow the search region of the map learned by the network, and prompt this map to evolve towards the actual ultrasound elastography process. (b) Traditional neural network methods cannot influence the intermediate state in the learning process, and thus may lead the learned map to be biased with the actual target map.

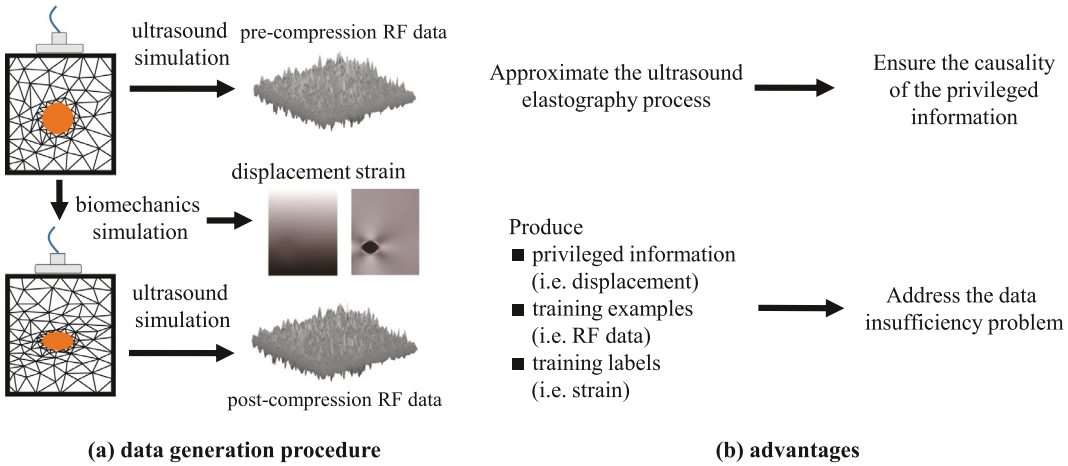

Fig. 5. Physically-based data generation in UE-LUPI. (a) The tissue displacement and strain are computed by the biomechanics simulation of the tissue deformation before and after the compression. The tissue deformation are then used as the digital phantoms to compute the pre- and post-compression RF data by the ultrasound simulation. (b) Two advantages of this data generation strategy: (1) ensure the causality of the privileged information with the training examples and labels in practice by approximating the ultrasound elastography process; (2) address the medical data insufficiency problem, and keep the rare clinical data for model validation rather than consuming them in the model training.

3.1.3. Enable to inference the intermediate state of the target map

Besides using the extra supervision information, UE-LUPI is capable to learn the intermediate state of the actual target map. According to Eq. (2), the causal privileged information Z contains the knowledge of the intermediate state of the target map $X \to Y$, but just having this causal condition cannot assure that the network learns the actual target map. This is because there may exist other unknown privileged information which also have the causality with the training examples and labels, i.e. $\exists X \to Z^k \to Y$ $(k = 1, 2, \ldots)$. This may lead the network evolves towards a biased learning direction because the single kind of privileged information contains the partial knowledge of the intermediate state of the target map.

Selecting the tissue displacement as the privileged information can address the problem of the incomplete intermediate state knowledge. According to the imaging principle of quasi-static ultrasound elastography (Ophir et al., 1991; Treece et al., 2011), the RF data (i.e. X) is used to compute the tissue displacement (i.e. Z), and the tissue displacement is used to compute the tissue strain (i.e. Y). It brings in the causal relationship $X \to Z \to Y$. Then, the tissue displacement is the necessary intermediate observation in the strain imaging process. Moreover, the tissue displacement can determine the tissue strain without the help of RF data, which has been validated by the gradient-based quasi-static methods (detailed in Section 2.2). Thus, the tissue displacement contains the sufficient information to inference the tissue strain. This characteristic leads the following proposition:

Proposition 1. *Denote the random variable of the input, privileged information and output in the learning model with LUPI paradigm as $\mathcal{X}$, $\mathcal{Z}$ and $\mathcal{Y}$, respectively. For the UE-LUPI, $\mathcal{X}$ and $\mathcal{Y}$ are conditionally independent on $\mathcal{Z}$, i.e. $\mathcal{X} \perp \mathcal{Y} | \mathcal{Z}$*

The conditional independence in Proposition 1 indicates that we can observe all information in Y from Z (Koller and Friedman, 2009), i.e. Z contains all information of the relationship between X and Y, and the remaining information in X not included in Z is not related to Y. Specific in the strain reconstruction task, the information in the RF data (X) related to the tissue strain (Y) are all included in tissue displacement (Z), and the tissue strain can be computed based on the displacement information without the need of the RF data. This property can satisfy the no-harm guarantee in the LUPI paradigm (Lambert et al., 2018), because this privileged information do not provide the redundant or incomplete knowledge to mislead the learning model. Accordingly, the privileged information can be constructed into a loss term to the intermediate layer of the neural network in our UE-LUPI. The form of the loss term can guide the network training by correcting the intermediate state of the learning process, and thus prompt the map learned by the network to evolve towards the actual ultrasound elastography.

3.1.4. Improve the strain reconstruction performance

By the conditional independence in Proposition 1, UE-LUPI can be considered to learn a map by two simple models (i.e. N_1 and N_2) instead of a complex model (i.e. the entire network). This characteristic leads the following proposition:

Proposition 2. *UE-LUPI can reduce the upper bound of the generalization error in the neural network.*

The generalization error of the learning model is the difference between the true error R and training error R_m, where the true error has the following Rademacher generalization bound with probability at least $1 - \delta$ (Bartlett and Mendelson, 2002):

$$R(h) \leqslant R_m(h) + 4M\mathfrak{R}_m(\mathcal{H}) + M^2\sqrt{\frac{\log \frac{1}{\delta}}{2m}} \tag{6}$$

where h is the map or function possibly learned by the network in the hypothesis space $\mathcal{H}$, m is the number of samples, $\mathfrak{R}_m$ is the Rademacher complexity that represents the model complexity. M is the upper bound of infinite norm between h and the true model. δ is a positive marginal constant.

Denote the Rademacher complexity of the traditional neural network as $\mathfrak{R}_m(\mathcal{H})$. In our UE-LUPI, the learning process of the neural network can be considered as consisting of two cascade processes (i.e. $X \to Z$ and $Z \to Y$). Thus, the Rademacher complexity of the entire network can be represented as $\mathfrak{R}_m(\mathcal{H}_1) + \mathfrak{R}_m(\mathcal{H}_2)$, where $\mathcal{H}_1$ and $\mathcal{H}_2$ are hypothesis space corresponding to the two cascade processes. Because the Rademacher complexity grows exponentially with the depth of the neural network, the network in UE-LUPI has lower Rademacher complexity (i.e. $\mathfrak{R}_m(\mathcal{H}_1) + \mathfrak{R}_m(\mathcal{H}_2) < \mathfrak{R}_m(\mathcal{H})$). The reduction of the Rademacher complexity can reduce the Rademacher generalization bound shown in Eq. (6). This indicates the difference between the true error and training error of the network decreases (i.e. reduce the generalization error) and thus reduce the model variance. The detailed theoretical

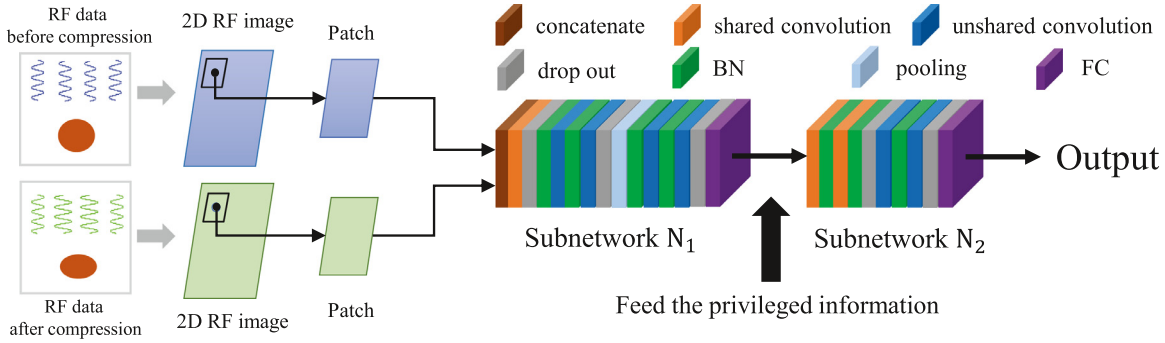

Fig. 6. The network details in UE-LUPI.

analysis of Proposition 2 is shown in Appendix A. Therefore, UE-LUPI can improve the performance of the neural network in the strain reconstruction task.

3.1.5. Implementation in the strain reconstruction task

The network architecture in UE-LUPI can be considered as the combination of two cascade subnetworks (N_1 and N_2) corresponding to the RF-to-displacement map and displacement-to-strain map, respectively. The input of entire network are two sets of 2D RF data (denoted by R_1 and R_2) collected before and after compressing the target tissue. Fig. 6 shows the network details. The subnetwork N_1 firstly adopts the separable convolution to obtain the feature maps of R_1 and R_2 independently and concatenate them. Then, the high-level contextual information is extracted by locally-connected convolution (LCC) from this concatenated feature map to represent the difference between R_1 and R_2 (Chollet, 2017). The feature map is further represented by dropout, batch normalization (BN), LCC, BN, LCC, dropout, BN, LCC, BN, LCC, and dropout in sequence. Finally, the 2D feature map are resized into a vector and then fed into a three-layer fully-connected network (64, 32 and 1 units for three layers). The subnetwork N_2 is composed of the convolution, BN, convolution, BN, dropout, LCC, BN, LCC and dropout in sequence. Similar to N_1, a fully-connected network is finally used to predict the strain from the vectorized feature produced by the preceding layers.

UE-LUPI trains the network only on simulation data and tests it simulation, phantom and real clinical data. Then a part-to-whole training procedure in order to reduce the gradient vanishing influence in the shadow layers of the network. In this part-to-whole training procedure, UE-LUPI firstly trains the N_1 and N_2 independently. The loss functions of N_1 (denoted by L_1) and N_2 (denoted by L_2) is formulated as $L_1 = \sum_{i=1}^{M_1} \sum_{j \in I_1} ||D_{i,j} - D^g_{i,j}||$ and $L_2 = \sum_{i=1}^{M_2} \sum_{j \in I_2} ||S_{i,j} - S^g_{i,j}||$, where $D_{i,j}$ and $S_{i,j}$ are the displacement and strain values at (i, j) estimated by N_1 and N_2, respectively. $D^g_{i,j}$ and $S^g_{i,j}$ are corresponding ground truth. M_1 and M_2 are the patch numbers. I_1 and I_2 are the patch regions. Then, UE-LUPI train the entire network by simultaneously using the privileged information and the training labels. The loss function in Eq. (5) can be rewritten as $loss = L_1 + L_2$.

3.2. Physically-based data generation for ensuring the causality of the privileged information

For assuring the causality of the privileged information with the training examples and labels, UE-LUPI proposes a strategy to generate the triplets of the RF data, tissue displacement and strain labels by numerical simulation. This causality comes from the tissue biomechanics and ultrasound physics used in the numerical simulation which can prompt the data generation process to approximate the actual ultrasound elastography process. Moreover, it can endow the UE-LUPI with conditional independence between the training examples and labels on the privileged information (see Proposition 1). In addition, it can address the model overfitting due to data insufficiency, as well as use all clinical data to validate the model in avoidance of consuming them in the model training.

Specified in the strain reconstruction task, the proposed data generation aims to generate the synthetic pre- & post-compression RF data with displacement data and strain tags for network training (see Fig. 5). In the numerical simulation, the tissue compression process is the perpendicular compression of skin by a cylindrical and flat-ended indentor. The soft tissue is assumed to be homogeneous and isotropic. Based on these assumptions, we can use the finite element model (mesh the tissue into by massive nodes) to describe the deformation within the soft tissue under compression, and compute the spatial locations of the nodes. The change of the node location in the tissue deformation can provide the displacement field and strain field that is considered as by the ground truth or the labels of the training data. Then, these nodes can be regarded as the scatter points in ultrasound simulation and thus form two kinds of digital phantoms, corresponding to the tissues before and after compression, respectively. According to Jensen and Svendsen (1992), we can compute the simulated RF signals from the pre- & post-compression digital phantoms, and then considered these RF signals as the network input in the training process.

4. Experiments and results

In this section, we have shown the effectiveness of our UE-LUPI in simulation, phantom and real clinical data, as well as the data collection, implementation details and evaluation indices.

4.1. Data collection

4.1.1. Simulation data

We produce 200 simulation tissues with 3 cm × 5 cm (width × depth) according to Section 3.2. In each simulation tissue, 10,000 scatter points are contained with pre-specified locations and an inclusion with random number of scatter points. The background and inclusions in the simulation tissue has different values of Young's module. The background is set 25 kPa, and the inclusions are set 8 kPa, 14 kPa, 45 kPa and 80 kPa. Then the commercially available software COMSOL 5.1 is used to calculate the position of all scattering points after compressing the tissue by the finite element method, as well as the ground truth of tissue displacement field and strain field. Finally, the 2D RF data of these scattering points before and after tissue compression is generated by an ultrasound simulation system Field II (Jensen, 1996). The central frequency and sampling frequency in Field II are set 6 MHz and 40 MHz, respectively.

Table 1
Better performance in simulation data of our framework (UE-LUPI) than four state-of-the-art methods.

	displacement		strain		
	SNR_d	$RMSE_d$ (μm)	SNR_e	CNR_e	$RMSE_s$
NCC	92.69 ± 8.59	3.407	10.78 ± 2.12	9.74 ± 7.82	4.202
OF	98.20 ± 8.92	2.898	23.05 ± 5.51	35.83 ± 7.22	1.605
AM-Kalman	102.75 ± 7.36	2.734	19.78 ± 2.63	33.95 ± 4.75	1.893
DL-US	96.07 ± 8.86	2.815	28.68 ± 6.80	62.32 ± 10.80	1.421
Our (UE-LUPI)	**106.57 ± 8.35**	**2.502**	**34.76 ± 7.45**	**70.45 ± 10.45**	**1.251**

4.1.2. Phantom data

We collect the phantom data from a commercially available elasticity QA phantom (CIRS049, Norfolk, VA, USA). Using a VerasonicsVantage 256 system (Verasonics Inc., WA, USA) equipped with an L12-5 transducer, we obtain the 2D RF data from 42 regions within this phantom, including four different inclusions with Young's module of 8 kPa, 14 kPa, 45 kPa and 80 kPa, as well as a background region with Young's module of 25 kPa. The central frequency and sampling frequency of the scanning are set 6.25 MHz and 40 MHz, respectively.

4.1.3. Real clinical data

We acquire the four real clinical data (one is for liver and the remaining are for breast) from a public dataset distributed by Rivaz et al. (2011).

4.2. Implementation details and evaluation indices

All input 2D RF arrays are resized to 2608×128 pixels in both training and testing stages. The patch sizes in the DRN and SRN are 71×9 and 61×9, respectively. In the training procedure, we use ADAM with the momentum 0.9 as the optimization algorithm. The iteration number is 30 epochs. The learning rate is 0.01. The training dataset contains 100 simulation tissues. The entire model for training and testing were implemented by TensorFlow on a NVIDIA GTX1070 GPU.

We apply the root-mean-square error (RMSE), as well as two relative indices, elastographic signal-to-noise ratio (SNR_e) and elastographic contrast-to-noise ratio (CNR_e), to measure the quality of the strain reconstruction (Srinivasan et al., 2003), because no ground truth can be obtained in phantom data and real clinical data:

$$\begin{aligned} SNR_e &= 10 \log \frac{e_i}{\sigma_i} \\ CNR_e &= 10 \log \frac{2(e_b - e_i)^2}{\sigma_b^2 + \sigma_i^2} \end{aligned} \tag{7}$$

where e_b and σ_b are the mean value and variance of the background, and e_i and σ_i the mean value and variance of the inclusion.

In order to show that UE-LUPI learns the actual ultrasound elastography process, we use the RMSE and the displacement signal-to-noise ratio (SNR_d) to measure the closeness between the output of the intermediate layer in the network and the generated displacement in simulation data. The SNR_d is formulated as:

$$SNR_d = (l_d - l_g)^2 / l_g^2 \tag{8}$$

where l_d and l_g are displacement profiles generated by our approach and the ground truth, respectively (Srinivasan et al., 2003).

4.3. Performance of UE-LUPI

Low RMSE and signal-to-noise ratio. Table 1 shows the high performance of UE-LUPI in strain reconstruction of simulation tissues, as well as the displacement estimation. In the strain reconstruction, the low value of RMSE (=1.251) indicates that UE-LUPI can reconstruct the strain field with low error with the ground truth. Moreover, the low values of SNR_e (34.76 ± 7.45 dB) and CNR_e (70.45 ± 10.45 dB) imply that the strain field in the inclusion is less disturbed by noise, as well as the strain contrast between the background and the inclusion has a high-level signal-to-noise ratio. In addition, in the displacement computation, the SNR_d is 106.57 ± 8.35 dB and the RMSE is 0.09. These results show that the error of the displacement field estimated by UE-LUPI is at a low level.

High agreement. Fig. 7 displays that UE-LUPI is highly agreed with the ground truth in all simulation data by the Bland-Altman

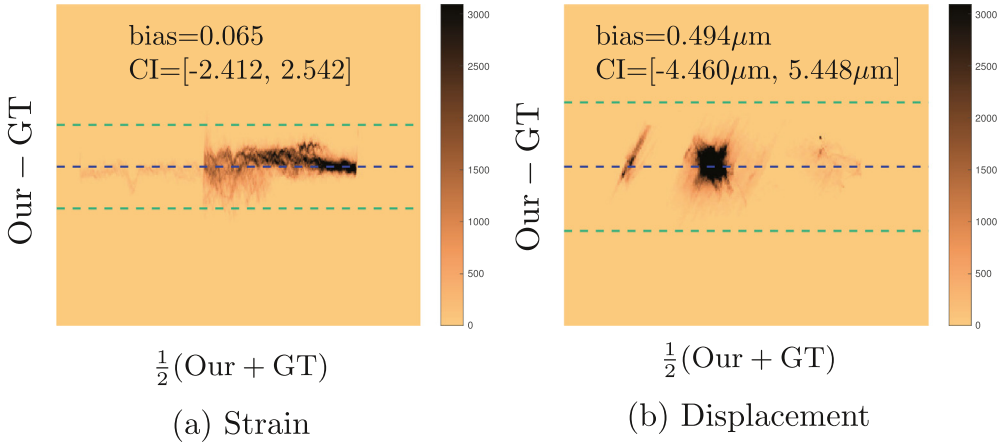

Fig. 7. High agreement between our framework ("Our") and the ground truth ("GT") evaluated by the Bland-Altman analysis (BA). (a) The results of strain reconstruction. (b) The results of displacement computation. The blue dashed lines are the average values of the bias between the results from our UE-LUPI and the ground truth. The green dashed lines show the 95% confidence interval (CI). The different colors indicate the different density or the frequency of the scatter points in the two-dimensional BA planes. The correspondence between the color and the density are displayed in the color bars. The strain results in BA plots have no unit. (For interpretation of the references to color in this figure legend, the reader is referred to the web version of this article.)

Table 2
Better performance in phantom and patient data of our framework (UE-LUPI) than four state-of-the-art methods.

	Phantom data		Patient data	
	SNR_e	CNR_e	SNR_e	CNR_e
NCC	21.34 ± 5.53	31.66 ± 23.19	16.47 ± 3.45	29.44 ± 10.49
OF	27.53 ± 4.71	41.83 ± 9.92	21.36 ± 5.53	31.66 ± 23.19
AM-Kalman	29.60 ± 4.02	38.21 ± 14.86	9.63 ± 12.84	36.22 ± 24.98
DL-US	32.55 ± 5.05	45.16 ± 11.23	23.26 ± 3.20	40.35 ± 18.38
Our (UE-LUPI)	$\mathbf{36.56 \pm 3.83}$	$\mathbf{48.65 \pm 11.43}$	$\mathbf{30.44 \pm 5.13}$	$\mathbf{47.13 \pm 20.98}$

(BA) analysis (Bland and Altman, 1986). The left and right plots show the results of tissue strain and displacement, respectively. The different colors indicate the different density or the frequency of the scatter points in the two-dimensional BA planes. For the strain reconstruction, the average bias of our results with respect to the ground truth is 0.065 with 95% confidence interval [−2.412, 2.542] in Bland-Altman analysis. For the displacement computation, this bias is 0.494 µm with 95% confidence interval [−4.460, 5.448].

4.4. Outperformance over the state-of-the-art methods

The superiority of UE-LUPI has been shown in simulation, phantom and real clinical data by comparing with four state-of-the-art methods: NCC (Luo and Konofagou, 2010), OF (Pan et al., 2015), AM-Kalman (Rivaz et al., 2011) and DL-US (Wu et al., 2018). NCC computed the maximum normalized cross-correlation value between the measurement window and the best-matched window for estimating the tissue displacement, and then used the gradient method to obtain the tissue strain. OF used the brightness constancy assumption in the optical flow model to constrain the motion of the measurement window for estimate tissue displacement, and then utilized the gradient method to compute the tissue strain. AM-Kalman applied 2D analytic minimization to obtain the tissue displacement from RF data and then used the Kalman filter to calculate the smooth strain field. DL-US adopted two neural networks to estimate the displacement field from RF data and the strain field from the displacement field, respectively. The parameters used in these state-of-the-art methods are identical with those provided in their publications.

4.4.1. Higher performance in simulation data

Table 1 displays that the outperformance of UE-LUPI to the state-of-the-art methods in the simulation data. The higher SNR and lower RMSE indicate that UE-LUPI is better than DL-US in the strain reconstruction and displacement computation (6.08 dB higher for SNR_e, 8.13 dB higher for CNR_e, and 0.170 lower for the strain RMSE; 10.5 dB higher for SNR_d and 0.313 µm lower for the displacement RMSE). Although in our preliminary study (Wu et al., 2018), DL-US shows slightly worse than AM-Kalman (6.68 dB lower for SNR_d and 0.081 µm higher for displacement RMSE), the improvement of UE-LUPI with respect to DL-US causes that UE-LUPI shows better performance than AM-Kalman (3.82 dB higher for SNR_d and 0.232 µm lower for displacement RMSE). UE-LUPI is also superior to AM-Kalman in the strain reconstruction. Besides, UE-LUPI performs much better than NCC and OF in both strain reconstruction and displacement computation. These results show that UE-LUPI is better than these state-of-the-art methods.

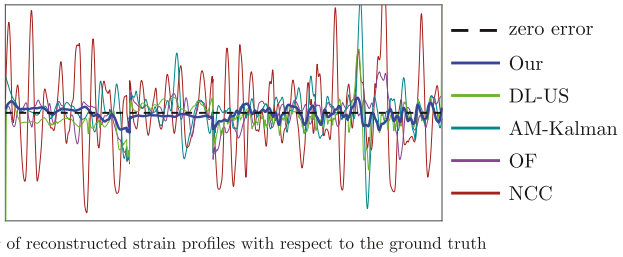

Fig. 8. Better performance of our framework (UE-LUPI) than the four comparative methods by displaying the representative results of strain profile. The curve plot displays the errors of the estimated strain profiles and the ground truth in simulation data. It shows that our framework (blue curves) have smaller error to the ground truth (black dashed line) than NCC (brown), OF (purple), AM-Kalman (dark cyan) and DL-US (green). It originates from the lower values of RMSE value and higher values of SNR_d by the UE-LUPI. (For interpretation of the references to color in this figure legend, the reader is referred to the web version of this article.)

4.4.2. Higher performance in phantom and real clinical data

Table 2 shows the performance of UE-LUPI is better than the other methods in phantom data (the increase of $SNR_e \geqslant 4.01$ dB and $CNR_e \geqslant 3.49$ dB), as well as in real clinical data (the increase of $SNR_e \geqslant 7.18$ dB and $CNR_e \geqslant 6.78$ dB).

4.4.3. Higher performance visualized in the representative data

Fig. 8 illustrates the higher strain reconstruction performance of UE-LUPI than the other methods by visualizing a representative simulation data. The results indicate that UE-LUPI (blue curves) can predict the strain field closer to the ground truth than NCC (brown), OF (purple), AM-Kalman (dark cyan), and DL-US (green). Besides, UE-LUPI has the highest lesion-background contrast and the most homogeneous strain field in all of these methods Figs. 9 and 10.

Fig. 11 illustrates the higher strain reconstruction performance of UE-LUPI than the comparative methods by visualizing a representative phantom data and a representative real clinical data. The strain field reconstructed by UE-LUPI has better performance on lesion-background contrast and surface homogeneity than these comparative methods.

4.4.4. Higher effectiveness-to-efficiency ratio

UE-LUPI has higher effectiveness-to-efficiency ratio (i.e. the ratio of the evaluation index to the computational time) than all comparative methods. The effectiveness-to-efficiency ratio of NCC is considered as the baseline value because NCC, as the first classic ultrasound elastography method (Ophir et al., 1991), has been widely used in the method comparison in the literature (e.g. Amidabadi et al., 2018; Hashemi and Rivaz, 2017; Shaswary et al., 2016; Pan et al., 2015). For simulation data, the average improvement rates of the effectiveness-to-efficiency ratio (the unit is dB/second) with respect to SNR_e (CNR_e) are 671% (1631%), 506% (1357%), 368% (790%), 58% (172%) in our UE-LUPI, DL-US, AM-Kalman, OF, respectively. For phantom data, these improvement rates are 308% (266%), 250% (227%), 300% (248%), −10% (−8%). For real clinical data, these improvement rates are 540% (455%), 347% (333%), 116% (355%), −27% (−39%). These results can indicate that UE-LUPI can obtain the high-quality strain images when preserving the high computational efficiency.

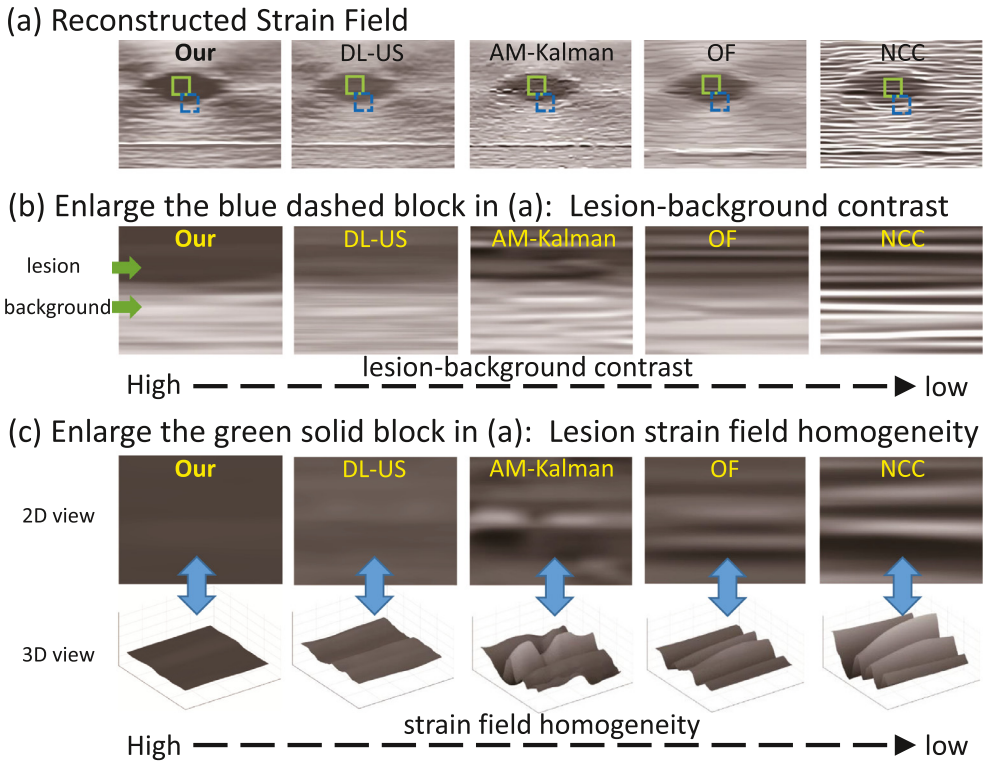

Fig. 9. Better performance of our framework (UE-LUPI) than the four comparative methods by displaying the representative results of strain fields in simulation data. (a) shows the completed strain fields. (b) shows the lesion-background contrast in the partial enlargement of blue dashed blocks in (a). (c) shows the image homogeneity and its 3D visualization in the partial enlargement of green blocks in (a). These results present that the strain field estimated by our framework from simulation data has higher lesion-background contrast and more homogeneous appearance than these comparative methods. (For interpretation of the references to color in this figure legend, the reader is referred to the web version of this article.)

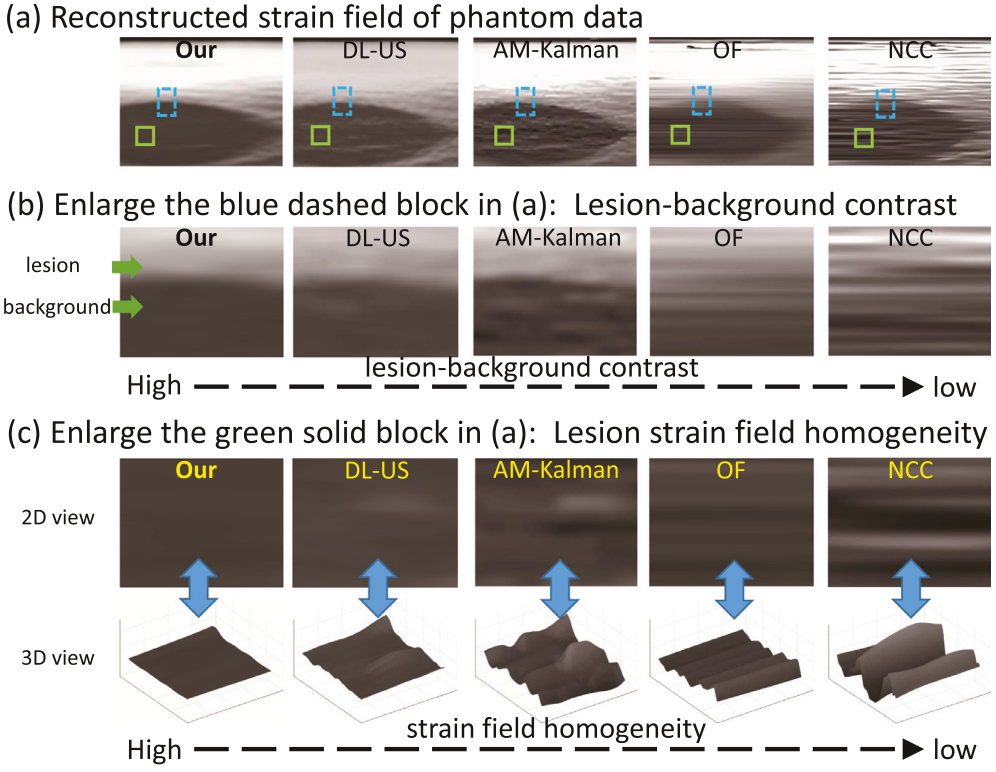

Fig. 10. Better performance of our framework (UE-LUPI) than the four comparative methods by displaying the representative results of strain fields in phantom data. (a) shows the completed strain fields. (b) shows the lesion-background contrast in the partial enlargement of blue dashed blocks in (a). (c) shows the image homogeneity and its 3D visualization in the partial enlargement of green blocks in (a). These results present that the strain field estimated by our framework from phantom data has higher lesion-background contrast and more homogeneous appearance than these comparative methods. (For interpretation of the references to color in this figure legend, the reader is referred to the web version of this article.)

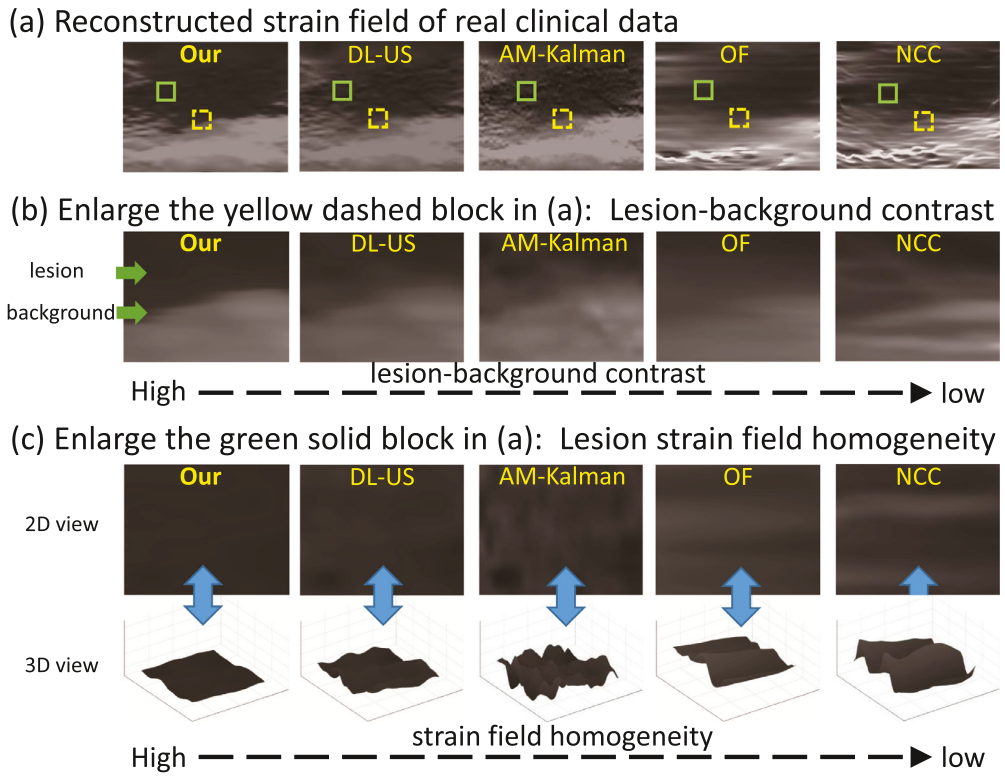

Fig. 11. Better performance of our framework (UE-LUPI) than the four comparative methods by displaying the representative results of strain fields in real clinical data. (a) shows the completed strain fields. (b) shows the lesion-background contrast in the partial enlargement of yellow dashed blocks in (a). (c) shows the image homogeneity and its 3D visualization in the partial enlargement of green blocks in (a). These results present that the strain field estimated by our framework from real clinical data has higher lesion-background contrast and more homogeneous appearance than these comparative methods. (For interpretation of the references to color in this figure legend, the reader is referred to the web version of this article.)

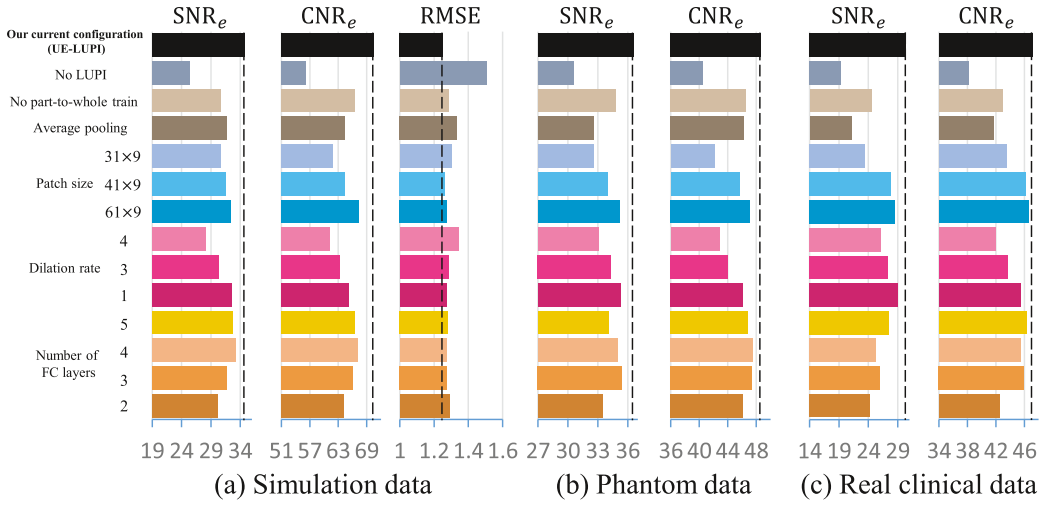

Fig. 12. Effectiveness of the UE-LUPI's components in tissue strain reconstruction on (a) simulation data, (b) phantom data and (c) real clinical data. In the ablation study, we evaluate the different configurations of the network architecture, including not using causal privileged information (light gray blue), not using part-to-whole training scheme (light bisque), using average pooling strategy (dark bisque), patch size (=31 × 9: light sky blue ; =41 × 9: deep sky blue ; =61 × 9: dark blue), dilated rate of the convolution kernel (=4: pale red ; =3: light red ; =2: dark red), number of FC layers (=5: gold ; =4: orange ; =2: light tan ; =1: dark tan). The better results show the effectiveness of the current configurations of UE-LUPI (shown in black), which applies the causal privileged information, part-to-whole training and max pooling, with dilation rate=1, patch size=71 × 9 and FC layers=3. (For interpretation of the references to color in this figure legend, the reader is referred to the web version of this article.)

4.5. Effectiveness of the network configuration in UE-LUPI

The performance of different network components in UE-LUPI are shown by the ablation study (Girshick et al., 2014). Fig. 12 shows the results of the ablation study. Firstly, The results indicate the current configurations of the proposed network architecture (the pooling strategy, layer number, dilated rate of the convolution kernel, and patch size) are effective. Then, the part-to-whole training strategy is replaced by the direct training (i.e. without training two subnetworks in UE-LUPI independently). The results show that the SNR$_d$, SNR$_e$ and CNR$_e$ decrease and the RMSE increase in both strain reconstruction and displacement computation. Moreover, the

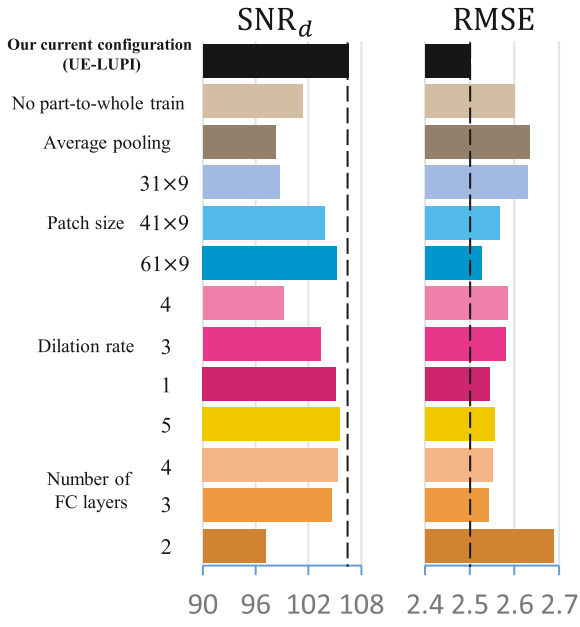

Fig. 13. Effectiveness of the UE-LUPI's components in tissue displacement computation. In the ablation study, we evaluate the different configurations of the network architecture, including not using part-to-whole training scheme (light bisque), using average pooling strategy (dark bisque), patch size (=31 × 9: light sky blue ; =41 × 9: deep sky blue ; =61 × 9: dark blue), dilated rate of the convolution kernel (=4: pale red ; =3: light red ; =2: dark red), number of FC layers (=5: gold ; =4: orange ; =2: light tan ; =1: dark tan). The better results show the effectiveness of the current configurations of UE-LUPI (shown in black), which applies the causal privileged information, part-to-whole training and max pooling, with dilation rate=1, patch size=71 × 9, FC layers=3. (For interpretation of the references to color in this figure legend, the reader is referred to the web version of this article.)

LUPI learning paradigm is removed in UE-LUPI. The results present that SNR$_e$ and CNR$_e$ largely decrease (9.39 dB and 14.21 dB for simulation data, 6.02 dB and 8.11 dB for phantom data, 11.14 dB and 8.96 dB for real clinical data) when only preserving the supervision on the output layer of the network. All these results can demonstrate the effectiveness of the LUPI learning paradigm, the current network configuration, and the part-to-whole training procedure in UE-LUPI for strain reconstruction Fig. 13.

4.6. Influence from simulation parameters of the physically-based data generation on UE-LUPI

The effectiveness of the current configuration in the proposed physically-based data generation are investigated in four aspects: the scatter amount, finite element size, Poisson's ratio and noise corruption.

First, the scatter amount is the number of scatter points used to produce the synthetic tissues in the numerical simulation. Table 3 shows that the UE-LUPI's performance decreases with the scatter amount (from 1×10^5 to 2×10^4) on simulation data, phantom data and real clinical data, where the scatter amount used in UE-LUPI is 1×10^5.

Then, the finite element size is the mesh density used in the finite element model for computing the deformation within the soft tissue under compression. Table 4 represents that the UE-LUPI's performance decreases when the finite element size increases (from 0.0005 dm to 0.01 dm), where the finite element size used in UE-LUPI is 0.0005 dm.

Finally, the Poisson's ratio is the negative of the ratio of transverse strain to axial strain of the tissue, which reflects the material characteristics of the synthetic tissue. Table 5 indicates that UE-LUPI performs well in the Poisson's ratio ranged between 0.4 and 0.5 (i.e. the range of human tissues).

4.7. Noise robustness of UE-LUPI

The noise influence of UE-LUPI is investigated by adding the extra gaussian noise to the RF signals in the training data and then the trained model is tested in simulation, phantom and real clinical data. Four values of the noise-to-signal ratio are set: 0.01, 0.02, 0.03 and 0.04. Table 6 shows that UE-LUPI performs better than all comparative methods even when the noise-to-signal ratio reaches 0.02. This can demonstrate the noise robustness of UE-LUPI.

5. Discussion

5.1. Contributions to clinical community

First, UE-LUPI is able to largely reduce the burden to the users in the tissue elasticity analysis by the quasi-static ultrasound elastography. Because of the high effectiveness-to-efficiency ratio, UE-LUPI can enable the users to sidestep the balance between the effectiveness first and the efficiency first, unlike those must be suffered when using the explicit strain reconstruction methods. Contributed to this sidestep, UE-LUPI is able to decrease the experience requirement for the users about the existing methods. Alternatively, only the network configuration are needed to be prespecified. Thus, UE-LUPI can help the inexperienced or fresh users to access the strain reconstruction task easily and rapidly.

Second, UE-LUPI can be readily transferred to other ultrasound elastography techniques, such as vibro-acoustography, transient elastography, and shear wave elasticity imaging. All of these techniques produce the visualization of the tissue elasticity distribution inherently based on the variation of RF signals with respect to the different biomechanical properties of tissues. Thus, the elasticity reconstruction problem in these methods can be considered as an inference problem, where the input signals are all RF data and output targets are elasticity-related index. When applying UE-LUPI to other ultrasound elastography methods, the training data and the labels only need to be simply replaced by those in the specified ultrasound elastography method. This potential versatility of UE-LUPI shows its value in clinical ultrasound elastography diagnosis, although UE-LUPI in this work aims at the widespread quasi-static technique (configured in the high-end ultrasound systems of all major manufacturers (Cosgrove et al., 2013)).

5.2. Contributions to medical imaging and machine learning community

We enable the use of the causal LUPI paradigm in network learning by our newly proposed framework for guiding the network to learn the actual target map. The core of this strategy is to provide causal privileged information to supervise the intermediate layer of the network for correcting the intermediate state of the learning process. By this strategy, it is considered that the learning process of the network can be divided into two simpler cascade subprocesses when the input and output of the learning model are conditionally independent on the its intermediate state. This behavior can narrow the search region of the network parameters owing to the decrease of the Rademacher complexity, and thus induce the map learned by the network to evolve towards the actual target map. It further decreases the upper bound of the generalization error and thus reduces the model variance of the network. Specified in the strain reconstruction task, the tissue displacement is a certain intermediate observation in the RF-to-strain process according to tissue biomechanics and ultrasound physics. Hence,

Table 6
Influence on our framework's performance from the training data generated under the gaussian noise with different noise-to-signal ratios.

		Noise-to-signal ratio (= 0 in the current configuration)				
		0	0.01	0.02	0.03	0.04
Simulation data	SNR_d	106.57 ± 8.35	106.55 ± 10.32	104.68 ± 8.97	103.59 ± 9.36	101.95 ± 11.15
	$RMSE_d$	2.502	2.561	2.579	2.85	3.178
	SNR_e	34.76 ± 7.45	32.09 ± 7.32	29.9 ± 7.59	27.01 ± 8.02	26.32 ± 8.42
	CNR_e	70.45 ± 10.45	68.76 ± 9.48	52.77 ± 10.33	45.12 ± 11.36	39.36 ± 11.62
	$RMSE_s$	1.251	1.297	1.906	2.446	2.617
Phantom data	SNR_e	36.56 ± 3.83	$36.44ca \pm 4.02$	32.62 ± 2.91	28.73 ± 2.53	27.22 ± 3.04
	CNR_e	48.65 ± 11.43	49.31 ± 10.54	45.24 ± 11.04	44.07 ± 11.67	39.92 ± 12.72
Patient data	SNR_e	30.44 ± 5.13	29.27 ± 5.36	25.53 ± 4.81	24.23 ± 4.11	22.75 ± 5.57
	CNR_e	47.13 ± 20.98	47.37 ± 18.66	44.65 ± 18.43	35.59 ± 15.82	31.68 ± 20.12

Table 3
Influence on our framework's performance from the training data generated under the different scatter amounts. The current scatter amount is 100,000.

		Scatter amount (= 100,000 in the current configuration)				
		100,000	80,000	60,000	40,000	20000
Simulation data	SNR_d	106.57 ± 8.35	106.32 ± 7.99	106.09 ± 7.07	105.31 ± 8.35	102.45 ± 7.82
	$RMSE_d$	2.502	2.513	2.561	2.892	3.019
	SNR_e	34.76 ± 7.45	34.53 ± 7.41	33.72 ± 5.56	29.86 ± 6.16	28.23 ± 6.62
	CNR_e	70.45 ± 10.45	70.34 ± 10.49	69.17 ± 9.81	57.18 ± 10.98	45.04 ± 10.02
	$RMSE_s$	1.251	1.253	1.695	2.389	2.512
phantom data	SNR_e	36.56 ± 3.83	35.64 ± 3.57	34.26 ± 4.83	32.02 ± 4.92	30.73 ± 4.41
	CNR_e	48.65 ± 11.43	48.28 ± 10.76	45.45 ± 11.55	39.58 ± 10.45	39.05 ± 12.03
patient data	SNR_e	30.44 ± 5.13	29.25 ± 3.48	27.69 ± 4.37	25.02 ± 5.14	23.47 ± 4.98
	CNR_e	47.13 ± 20.98	45.04 ± 18.21	41.86 ± 18.84	37.34 ± 18.25	35.76 ± 16.65

Table 4
Influence on our framework's performance from the training data generated under the different finite element sizes.

		Finite element size (= 0.0005 in the current configuration)			
		0.0005	0.001	0.005	0.01
Simulation data	SNR_d	106.57 ± 8.35	106.50 ± 7.77	104.14 ± 8.32	102.01 ± 8.86
	$RMSE_d$	2.502	2.570	2.994	3.187
	SNR_e	34.76 ± 7.45	33.25 ± 8.37	31.56 ± 8.18	29.97 ± 7.88
	CNR_e	70.45 ± 10.45	66.39 ± 10.27	61.64 ± 9.37	46.78 ± 9.69
	$RMSE_s$	1.251	1.547	1.994	2.271
Phantom data	SNR_e	36.56 ± 3.83	33.37 ± 3.02	31.6 ± 4.72	28.97 ± 5.28
	CNR_e	48.65 ± 11.43	46.94 ± 11.51	42.77 ± 12.58	41.92 ± 12.58
Patient data	SNR_e	30.44 ± 5.13	29.59 ± 5.82	27.08 ± 5.01	23.28 ± 6.33
	CNR_e	47.13 ± 20.98	45.70 ± 19.96	40.85 ± 21.12	37.93 ± 21.90

Table 5
Influence on our framework's performance from the training data generated under the different values of Poisson's ratio.

		Poisson's ratio (= 0.45 in the current configuration)				
		0.45	0.46	0.47	0.48	0.49
Simulation data	SNR_d	106.57 ± 8.35	106.56 ± 7.7	106.55 ± 7.59	106.35 ± 7.97	106.10 ± 8.25
	$RMSE_d$	2.502	2.466	2.513	2.732	2.944
	SNR_e	34.76 ± 7.45	34.62 ± 7.17	34.38 ± 7.04	33.64 ± 8.35	33.94 ± 8.67
	CNR_e	70.45 ± 10.45	70.52 ± 8.99	70.36 ± 9.74	68.10 ± 10.91	66.69 ± 11.33
	$RMSE_s$	1.251	1.256	1.254	1.378	1.575
Phantom data	SNR_e	36.56 ± 3.83	36.26 ± 4.87	36.38 ± 3.92	35.09 ± 5.65	34.47 ± 4.50
	CNR_e	48.65 ± 11.43	47.59 ± 11.14	48.23 ± 12.37	46.64 ± 10.62	45.32 ± 10.79
Patient data	SNR_e	30.44 ± 5.13	30.69 ± 3.49	29.51 ± 4.61	29.02 ± 3.73	26.34 ± 3.95
	CNR_e	47.13 ± 20.98	46.27 ± 18.75	46.41 ± 19.03	47.17 ± 20.57	45.42 ± 18.41

using tissue displacement as the privileged information can naturally lead the network to learn from the physical causality among RF data, tissue displacement and strain. This strategy can be accessibly applied to any neural network architecture because it is independent on the architecture details.

We perform a pioneer study of inferring the physical properties of soft tissue from raw physical signals using machine learning. This research direction has not been well established in imaging the elasticity of soft tissue, although a few studies have estimated the elasticity-related physiological indicators from the B-mode ultrasound imaging (Gao et al., 2018a, 2017, 2018b, 2015, 2016; Zhao et al., 2018), as well as have investigated the imaging process of tissue by machine learning in MRI and CT (Schlemper et al., 2018, 2017; Chen et al., 2017; Würfl et al., 2016; Xu et al., 2018). In one

of embodiments in this research direction, we have developed a framework to infer the tissue strain from pre- & post-compression RF data. Our study inherently aims to solve an attractive machine learning problem applied in a medical imaging scenario: how to infer the biomechanical properties which are difficult to be directly observed from the physical signals.

5.3. Reasons for UE-LUPI validity

Two goals in the framework design ensure that UE-LUPI has the superiority in solving the strain reconstruction task.

First, a reasonable learning mechanism should be proposed to learn the relationship among the RF data and tissue strain. To achieve this goal, we are the first to use the deep neural network to extract the strain-related features from RF data. The choice of the deep neural network is motivated by its effectiveness in the feature learning that has been proved in the literature (Schmidhuber, 2015). Then, we propose a causal privileged information to help the network to learn the actual ultrasound elastography process. This strategy enables to correct the intermediate state in the learning process by formulating this privileged information as the loss term to supervise the intermediate layer of the network. The causality of the privileged information with the training examples and labels originates from their physical relationship. This can induce the network to gradually learn from the tissue biomechanics and ultrasound physics behind the RF-to-strain map.

Second, a reasonable data generation mechanism should be developed to assure the physical causality among the training examples, privileged information and training labels. This requirement comes from the fact that no direct measurement technique is capable to obtain the training labels (i.e. strain tags) and privileged information (i.e. displacement tags) in strain reconstruction. i.e. all the strain and displacement observations in clinical practice are estimated by the existing explicit ultrasound elastography methods. Besides, it is unsuitable to use the results of these existing methods as the privileged information and training data for network learning owing to the incapability to assure the inner physical relationship in ultrasound elastography. To achieve this goal, our data generation strategy is based on tissue-biomechanical and ultrasound-physical simulation. This strategy leads the generation process of the privileged information and training data to approximate the actual ultrasound elastography process and not rely on the existing reconstruction methods. In addition, it can address the data insufficiency problem in the ultrasound elastography in the network training, as well as preserve the rare clinical data for the network testing. Accordingly, the network trained by our data generation strategy is applicable to the real scenario.

6. Conclusion

In this study, we develop an implicit framework (UE-LUPI) using the deep neural network to reconstruct the strain field in quasi-static ultrasound elastography. The implicitness of UE-LUPI improve the user friendliness, model adaptation, and effectiveness-efficiency ratio. To ensure the suitability of UE-LUPI to the strain reconstruction task, the causal privileged information is proposed to correct the intermediate state in the learning process for directly guiding the internal feature representation. It can prompt the map learned by the network to evolve towards the actual ultrasound elastography process. Besides, the data generation strategy based on tissue biomechanics and ultrasound physics in UE-LUPI is proposed to approximate the actual ultrasound elastography process. It can ensure the causality of the privileged information and address the problem of training data insufficiency. The experimental results demonstrate the effectiveness of UE-LUPI for the strain reconstruction task in simulation, phantom and real clinical data.

Acknowledgments

This work was supported in part by the National Natural Science Foundation of China (61771464, U1801265), Science and Technology Planning Project of Guangdong Province (2018A050506031, 2019B010110001), and Guangdong Provincial Key Laboratory of Sensor Technology and Biomedical Instrument.

Conflicts of interest

None.

Appendix A. Theoretical analysis of Proposition 2

Denote x, z and y as the input, intermediate state and output of the network in UE-LUPI. The standard network aims to learn the map $x \to y$ (i.e. the function $y = f(x)$), while our network aims to learn the map $x \to z \to y$, (i.e. the function $z = f^{(1)}(x)$ and $y = f^{(2)}(z)$).

According to the learning theory (Vapnik, 1998), the true risk $R(h)$ and the empirical risk $R_n(h)$ of the learning model (e.g. neural network) can be formulated as

$$\text{True risk}: \ R(h) = E_x(h(x) - f(x))^2$$
$$\text{Empirical risk}: \ R_m(h) = \frac{1}{m}\sum_{i=1}^{m}(h(x_i) - f(x_i))^2 \tag{A.1}$$

where $h(x)$ is a hypothesis in the hypothesis space H, i.e. a function possibly learned by the network. $f(x)$ is desired function, m is the number of samples.

Then, the generalization error e_g of the learning model can be formulated as:

$$e_g = R(\hat{h}) - R_m(\hat{h}) \le \sup_h |R(h) - R_m(h)| \tag{A.2}$$

where $\hat{h} \in H$ is the function learned by the network on the finite sample set.

Assume $||h - f||_\infty \le M$ for all $h \in \mathcal{H}$. For any $\delta > 0$ and all $h \in \mathcal{H}$, the true risk of the learning model has the following Rademacher generalization bound with probability at least $1 - \delta$ (Bartlett and Mendelson, 2002; Kakade et al., 2008):

$$R(h) \le R_m(h) + 4M\mathfrak{R}_m(\mathcal{H}) + M^2\sqrt{\frac{\log\frac{1}{\delta}}{2m}} \tag{A.3}$$

The inequality in Eq. (A.3) can show the relationship between the true risk and empirical risk for the standard network.

For our network with the causal privileged information, denote $h^{(1)}$ and $h^{(2)}$ are the hypothesis corresponding to $f^{(1)}$ and $f^{(2)}$, respectively. The true risk $R'(\hat{h}^{(1)}, \hat{h}^{(2)})$ of our network can be formulated as:

$$\begin{aligned}
R'(\hat{h}^{(1)}, \hat{h}^{(2)}) &= E_{\hat{z},z}(\hat{h}^{(2)}(\hat{z}) - f^{(2)}(z))^2 \\
&= E_{\hat{z},z}(\hat{h}^{(2)}(\hat{z}) - \hat{h}^{(2)}(z) + \hat{h}^{(2)}(z) - f^{(2)}(z))^2 \\
&\le E_{\hat{z},z}(\hat{h}^{(2)}(\hat{z}) - \hat{h}^{(2)}(z))^2 + E_z(\hat{h}^{(2)}(z) - f^{(2)}(z))^2 \\
&\le E_{\hat{z},z}(\hat{z} - z)^2 + E_z(\hat{h}^{(2)}(z) - f^{(2)}(z))^2 \\
&= E_x(\hat{h}^{(1)}(x) - f^{(1)}(x))^2 + E_z(\hat{h}^{(2)}(z) - f^{(2)}(z))^2 \\
&\le \left(R_n^{(1)}(\hat{h}^{(1)}) + 4M\mathfrak{R}_m(\mathcal{H}_1) + M^2\sqrt{\tfrac{\log\frac{1}{\delta}}{2m}}\right) \\
&\quad + \left(R_n^{(2)}(\hat{h}^{(2)}) + 4M\mathfrak{R}_m(\mathcal{H}_2) + M^2\sqrt{\tfrac{\log\frac{1}{\delta}}{2m}}\right)
\end{aligned} \tag{A.4}$$

Thus, this true risk can be rewritten as

$$R'(h) \leq R'_m(h) + 4M(\mathfrak{R}_m(\mathcal{H}_1) + \mathfrak{R}_m(\mathcal{H}_2)) + c \tag{A.5}$$

where R'_n is the empirical risk and c is a constant.

Owing to the conditional independence between x and y on z, UE-LUPI can divide the learning process of the entire network into two cascade subprocesses without increasing the prediction error. Each subprocess has lower Rademacher complexity (i.e. $\mathfrak{R}_m(\mathcal{H}_1) < \mathfrak{R}_m(\mathcal{H})$ and $\mathfrak{R}_m(\mathcal{H}_2) < \mathfrak{R}_m(\mathcal{H})$) as it corresponds to the network with smaller size. Since the Rademacher complexity grows exponentially with the depth of the neural network at the worst case (Zhang et al., 2017; Sokolic et al., 2016; Golowic et al., 2018; Neyshabur et al., 2015), we have $\mathfrak{R}_m(\mathcal{H}_1) + \mathfrak{R}_m(\mathcal{H}_2) < \mathfrak{R}_m(\mathcal{H})$.

Combining it with Eqs. (A.2), (A.3) and (A.5), we have

$$R'(\hat{h}^{(1)}, \hat{h}^{(2)}) - R'_n(\hat{h}^{(1)}, \hat{h}^{(2)}) < R(h) - R_n(h) \tag{A.6}$$

This inequality indicates that UE-LUPI can reduce the generalization error of the network.

References

Amidabadi, M.G., Ahmad, M.O., Rivaz, H., 2018. Supervised classification of the accuracy of the time delay estimation in ultrasound elastography. IEEE Trans. Ultrason. Ferroelectr. Frequency Control 65 (1), 21–29.

Bamber, J., Cosgrove, D., Dietrich, C.F., Fromageau, J., Bojunga, J., Calliada, F., Cantisani, V., Correas, J.M., Onofrio, M.D., Drakonaki, E.E., Fink, M., Friedrich-Rust, M., Gilja, O.H., Havre, R.F., Jenssen, C., Klauser, A.S., Ohlinger, R., Saftoiu, A., Schaefer, F., Sporea, I., Piscaglia, F., 2013. EFSUMB guidelines and recommendations on the clinical use of ultrasound elastography. Part 1: Basic principles and technology. Ultraschall Med. 34, 169–184.

Barr, R.G., Cosgrove, D., Brock, M., Cantisani, V., Correas, J.M., Postema, A.W., Salomon, G., Tsutsumi, M., Xu, H.X., Dietrich, C.F., 2017. WFUMB guidelines and recommendations for clinical use of ultrasound elastography: Part 5: Prostate. Ultrasound Med. Biol. 43 (1), 27–48.

Barr, R.G., Nakashima, K., Amy, D., Cosgrove, D., Farrokh, A., Schafer, F., Bamber, J.C., Castera, L., Choi, B.I., Chou, Y.H., Dietrich, C.F., Ding, H., Ferraioli, G., Filice, C., Friedrich-Rust, M., Hall, T.J., Nightingale, K.R., Palmeri, M.L., Shiina, T., Suzuki, S., Sporea, I., Wilson, S., Kudo, M., 2015. WFUMB guidelines and recommendations for clinical use of ultrasound elastography: Part 2: Breast. Ultrasound Med. Biol. 41 (5), 1148–1160.

Bartlett, P.L., Mendelson, S., 2002. Rademacher and Gaussian complexities: risk bounds and structural results. J. Mach. Learn. Res. (3) 463–482.

Bisla, D., Choromanska, A., 2018. Visualbackprop for learning using privileged information with CNNs arXiv:1805.09474.

Bland, J.M., Altman, D.G., 1986. Statistical methods for assessing agreement between two methods of clinical measurement. Lancet 327 (8476), 307–310.

Brusseau, E., Kybic, J., Déprez, J.F., Basset, O., 2008. 2-D locally regularized tissue strain estimation from radio-frequency ultrasound images: theoretical developments and results on experimental data. IEEE Trans. Med. Imaging 27 (2), 145–160.

Chang, C.-C., Lin, C.H., Lee, C.-R., Juan, D.-C., Wei, W., Chen, H.-T., 2018. Escaping from collapsing modes in a constrained space. In: European Conference on Computer Vision (ECCV).

Chen, H., Zhang, Y., Kalra, M.K., Lin, F., Chen, Y., Liao, P., Zhou, J., Wang, G., 2017. Low-dose CT with a residual encoder-decoder convolutional neural network. IEEE Trans. Med. Imaging 36 (12), 2524–2535.

Chollet, F., 2017. Xception: deep learning with depthwise separable convolutions. In: IEEE Conference on Computer Vision and Pattern Recognition (CVPR), pp. 1251–1258.

Cosgrove, D., Barr, R., Bojunga, J., Cantisani, V., Chammas, M.C., Dighe, M., Vinayak, S., Xu, J.M., Dietrich, C.F., 2017. WFUMB guidelines and recommendations for clinical use of ultrasound elastography: Part 4: Thyroid. Ultrasound Med. Biol. 43 (1), 4–26.

Cosgrove, D., Piscaglia, F., Bamber, J., Bojunga, J., Correas, J.M., Gilja, O.H., Klauser, A.S., Sporea, I., Calliada, F., Cantisani, V., D'Onofrio, M., Drakonaki, E.E., Fink, M., Friedrich-Rust, M., Fromageau, J., Havre, R.F., Jenssen, C., Ohlinger, R., Sŏftoiu, A., Schaefer, F., Dietrich, C.F., 2013. EFSUMB guidelines and recommendations on the clinical use of ultrasound elastography. Part 2: Clinical applications. Ultraschall Med. 34, 238–253.

DiBattista, A., Noble, J.A., 2014. An efficient block matching and spectral shift estimation algorithm with applications to ultrasound elastography. IEEE Trans. Ultrason. Ferroelectr. Frequency Control 61 (3), 407–419.

Dong, S., Gao, Z., Sun, S., Wang, X., Li, M., Zhang, H., Yang, G., Liu, H., Li, S., 2018. Holistic and deep feature pyramids for saliency detection. In: British Machine Vision Conference (BMVC).

Duan, L., Xu, Y., Li, W., Chen, L., Wong, D.W.K., Wong, T.Y., Liu, J., 2014. Incorporating privileged genetic information for fundus image based glaucoma detection. In: International Conference on Medical Image Computing and Computer-Assisted Intervention (MICCAI), pp. 204–211.

Engel, J., Hoffman, M., Roberts, A., 2018. Latent constraints: learning to generate conditionally from unconditional generative models. In: International Conference on Learning Representations (ICLR).

Fearnhead, P., 2002. Markov chain Monte Carlo, sufficient statistics, and particle filters. J. Comput. Graph. Stat. 11 (4), 848–862.

Ferraioli, G., Filice, C., Castera, L., Choi, B.I., Sporea, I., Wilson, S.R., Cosgrove, D., Dietrich, C.F., Amy, D., Bamber, J.C., Barr, R., Chou, Y.H., Ding, H., Farrokh, A., Friedrich-Rust, M., Hall, T.J., Nakashima, K., Nightingale, K.R., Palmeri, M.L., Schafer, F., Shiina, T., Suzuki, S., Kudo, M., 2015. WFUMB guidelines and recommendations for clinical use of ultrasound elastography: Part 3: Liver. Ultrasound Med. Biol. 41 (5), 1161–1179.

Feyereisl, J., Kwak, S., Son, J., Han, B., 2014. Object localization based on structural SVM using privileged information. In: Twenty-Seventh Conference on Neural Information Processing Systems (NIPS), pp. 208–216.

Gao, Z., Li, Y., Sun, Y., Yang, J., Xiong, H., Zhang, H., Liu, X., Wu, W., Liang, D., Li, S., 2018. Motion tracking of the carotid artery wall from ultrasound image sequences: a nonlinear state-space approach. IEEE Trans. Med. Imaging 37 (1), 273–283.

Gao, Z., Sun, Y., Zhang, H., Ghista, D., Li, Y., Xiong, H., Liu, X., Xie, Y., Wu, W., Li, S., 2016. Carotid artery wall motion estimated from ultrasound imaging sequences using a nonlinear state space approach. In: International Conference on Medical Image Computing and Computer-Assisted Intervention (MICCAI), pp. 98–106.

Gao, Z., Xiong, H., Liu, X., Zhang, H., Ghista, D., Wu, W., Li, S., 2017. Robust estimation of carotid artery wall motion using the elasticity-based state-space approach. Med. Image Anal. 37, 1–21.

Gao, Z., Xiong, H., Zhang, H., Wu, D., Lu, M., Wu, W., Wong, K.K.L., Zhang, Y.T., 2015. Motion estimation of common carotid artery wall using a h_∞ filter based block matching method. In: International Conference on Medical Image Computing and Computer-Assisted Intervention (MICCAI), pp. 443–450.

Gao, Z., Zhang, H., Wang, D., Guo, M., Liu, H., Zhuang, L., Shi, P., 2018. Robust recovery of myocardial kinematics using dual $\mathcal{H}_\infty$ criteria. Multimed. Tools Appl. 77 (17), 23043–23071.

Gatys, L., Ecker, A.S., Bethge, M., 2015. Texture synthesis using convolutional neural networks. In: Twenty-ninth Conference on Neural Information Processing Systems (NIPS).

Gilks, W.R., Richardson, S., Spiegelhalter, D., 1995. Markov Chain Monte Carlo in practice. CRC Press.

Girshick, R., Donahue, J., Darrell, T., Malik, J., 2014. Rich feature hierarchies for accurate object detection and semantic segmentation. In: IEEE Conference on Computer Vision and Pattern Recognition (CVPR), pp. 580–587.

Golowic, N., Rakhlin, A., Shamir, O., 2018. Size-independent sample complexity of neural network. In: Thirty-first Annual Conference On Learning Theory (COLT).

Goudet, O., Kalainathan, D., Caillou, P., Guyon, I., Lopez-Paz, D., Sebag, M., 2018. Learning functional causal models with generative neural networks. In: Escalante, H.J., Escalera, S., Guyon, I., Baró, X., Güçlütürk, Y., Güçlü, U., van Gerven, M. (Eds.), Explainable and Interpretable Models in Computer Vision and Machine Learning. Springer, pp. 39–80.

Guo, Y., Liu, Y., Oerlemans, A., Lao, S., Wu, S., Lew, M.S., 2016. Deep learning for visual understanding: a review. Neurocomputing (187) 27–48.

Hasan, M.K., Anas, E.M.A., Alam, S.K., Lee, S.Y., 2012. Direct mean strain estimation for elastography using nearest-neighbor weighted least-squares approach in the frequency domain. Ultrasound Med. Biol. 38 (10), 1759–1777.

Hashemi, H.S., Rivaz, H., 2017. Global time-delay estimation in ultrasound elastography. IEEE Trans. Ultrason. Ferroelectr. Frequency Control 64 (10), 1625–1636.

Hjelm, R.D., Fedorov, A., Lavoie-Marchildon, S., Grewal, K., Bachman, P., Trischler, A., Bengio, Y., 2019. Learning deep representations by mutual information estimation and maximization. In: International Conference on Learning Representations (ICLR).

Hoerig, C., Ghaboussi, J., Insana, M.F., 2017. An information-based machine learning approach to elasticity imaging. Biomech. Model. Mechanobiol. 16 (3), 805–822.

Jensen, J.A., 1996. FIELD: a program for simulating ultrasound systems. In: 10th Nordicbaltic Conference on Biomedical Imaging, pp. 351–353.

Jensen, J.A., Svendsen, N.B., 1992. Calculation of pressure fields from arbitrarily shaped, apodized, and excited ultrasound transducers. IEEE Trans. Ultrason. Ferroelectr. Frequency Control 39 (2), 262–267.

Jiang, J., Hall, T.J., 2015. A coupled subsample displacement estimation method for ultrasound-based strain elastography. Phys. Med. Biol. 60 (21), 8347–8364.

Kakade, S.M., Sridharan, K., Tewari, A., 2008. On the complexity of linear prediction: risk bounds, margin bounds, and regularization. In: Twenty-second Conference on Neural Information Processing Systems (NIPS).

Kibria, G., Rivaz, H., 2018. GLUENet: ultrasound elastography using convolutional neural network. In: Stoyanov, D., Taylor, Z., Aylward, S., Tavares, J.M.R., Xiao, Y., Simpson, A., Martel, A., Maier-Hein, L., Li, S., Rivaz, H., Reinertsen, I., Chabanas, M., Farahani, K. (Eds.), Simulation, Image Processing, and Ultrasound Systems for Assisted Diagnosis and Navigation. Springer, pp. 21–28.

Koller, D., Friedman, N., 2009. Probabilistic Graphical Models: Principles and Techniques. The MIT Press.

Kuzmin, A., Zakrzewski, A.M., Anthony, B.W., Lempitsky, V., 2015. Multi-frame elastography using a handheld force-controlled ultrasound probe. IEEE Trans. Ultrason. Ferroelectr. Frequency Control 62 (8), 1486–1500.

Lambert, J., Sener, O., Savarese, S., 2018. Deep learning under privileged information using heteroscedastic dropout. In: IEEE Conference on Computer Vision and Pattern Recognition (CVPR), pp. 8886–8895.

Lapin, M., Hein, M., Schiele, B., 2014. Learning using privileged information: SVM+ and weighted SVM. Neural Netw. (53) 95–108.

Lee, C.Y., Xie, S., Gallagher, P.W., Zhang, Z., Tu, Z., 2015. Deeply-supervised nets. In: International Conference on Artificial Intelligence and Statistics (AISTATS), pp. 562–570.
Lu, M., Wu, D., Lin, W., Li, W., Zhang, H., Huang, W., 2014. A stochastic filtering approach to recover strain images from quasi-static ultrasound elastography. BioMed. Eng. OnLine 13, 1–17.
Luo, J., Konofagou, E.E., 2010. A fast normalized cross-correlation calculation method for motion estimation. IEEE Trans. Ultrason. Ferroelectr. Frequency Control 57 (6), 1347–1357.
Meng, F., Shi, J., Gong, B., Zhang, Q., Guo, L., Wang, D., Xu, H., 2018. B-mode ultrasound based diagnosis of liver cancer with CEUS images as privileged information. In: 40th Annual International Conference of the IEEE Engineering in Medicine and Biology Society (EMBC), pp. 3124–3127.
Neyshabur, B., Tomioka, R., Srebro, N., 2015. Norm-based capacity control in neural networks. In: Twenty-Eighth Annual Conference on Learning Theory (COLT).
Omidyeganeh, M., Xiao, Y., Ahmad, M.O., Rivaz, H., 2017. Estimation of strain elastography from ultrasound radio-frequency data by utilizing analytic gradient of the similarity metric. IEEE Trans. Med. Imaging 36 (6), 1347–1358.
Ophir, J., Céspedes, I., Ponnekanti, H., Yazdi, Y., Li, X., 1991. Elastography: a quantitative method for imaging the elasticity of biological tissues. Ultrason. Imaging 13 (2), 111–134.
Pan, X., Liu, K., Shao, J., Gao, J., Huang, L., Bai, J., Luo, J., 2015. Performance comparison of rigid and affine models for motion estimation using ultrasound radio-frequency signals. IEEE Trans. Ultrason. Ferroelectr. Frequency Control 62 (11), 1928–1943.
Pechyony, D., Vapnik, V., 2010. On the theory of learning with privileged information. In: Twenty-Fourth Conference on Neural Information Processing Systems (NIPS).
Pellot-Barakat, C., Frouin, F., Insana, M.F., Herment, A., 2004. Ultrasound elastography based on multiscale estimations of regularized displacement fields. IEEE Trans. Med. Imaging 23 (2), 153–163.
Rivaz, H., Boctor, E.M., Choti, M.A., Hager, G.D., 2011. Real-time regularized ultrasound elastography. IEEE Trans. Med. Imaging 30 (4), 928–945.
Rivaz, H., Boctor, E.M., Choti, M.A., Hager, G.D., 2014. Ultrasound elastography using multiple images. Med. Image Anal. 18, 314–329.
Rivaz, H., Foroughi, P., Fleming, I., Zellars, R., Boctor, E., Hager, G., 2009. Tracked regularized ultrasound elastography for targeting breast radiotherapy. In: International Conference on Medical Image Computing and Computer-Assisted Intervention (MICCAI), pp. 507–515.
Schlemper, J., Caballero, J., Hajnal, J.V., Price, A., Rueckert, D., 2017. A deep cascade of convolutional neural networks for mr image reconstruction. In: International Conference on Information Processing in Medical Imaging (IPMI), pp. 647–658.
Schlemper, J., Caballero, J., Hajnal, J.V., Price, A.N., Rueckert, D., 2018. A deep cascade of convolutional neural networks for dynamic MR image reconstruction. IEEE Trans. Med. Imaging 37 (2), 491–503.
Schmidhuber, J., 2015. Deep learning in neural networks: an overview. Neural Netw. 62 (1), 85–117.
Sharmanska, V., Quadrianto, N., Lampert, C.H., 2013. Learning to rank using privileged information. In: IEEE International Conference on Computer Vision (ICCV), pp. 825–832.
Sharmanska, V., Quadrianto, N., Lampert, C.H., 2014. Learning to transfer privileged information arXiv:1410.0389.
Shaswary, E., Xu, Y., Tavakkoli, J., 2016. Performance study of a new time-delay estimation algorithm in ultrasonic echo signals and ultrasound elastography. Ultrasonics 69, 11–18.
Shi, J., Xue, Z., Dai, Y., Peng, B., Dong, Y., Zhang, Q., Zhang, Y., 2018. Cascaded multi-column RVFL+ classifier for single-modal neuroimaging-based diagnosis of Parkinson's disease. IEEE Trans. Biomed. Eng. (in press).
Shi, Z., Kim, T.K., 2017. Learning and refining of privileged information-based RNNs for action recognition from depth sequences. In: IEEE Conference on Computer Vision and Pattern Recognition (CVPR), pp. 4684–4693.
Shiina, T., Nightingale, K.R., Palmeri, M.L., Hall, T.J., Bamber, J.C., Barr, R.G., Castera, L., Choi, B.I., Chou, Y.H., Cosgrove, D., Dietrich, C.F., Ding, H., Amy, D., Farrokh, A., Ferraioli, G., Filice, C., Friedrich-Rust, M., Nakashima, K., Schafer, F., Sporea, I., Suzuki, S., Wilson, S., Kudo, M., 2015. WFUMB guidelines and recommendations for clinical use of ultrasound elastography: Part 1: Basic principles and terminology. Ultrasound Med. Biol. 41 (5), 1126–1147.
Sokolic, J., Giryes, R., Sapiro, G., Rodrigues, M.R.D., 2016. Lessons from the rademacher complexity for deep learning. In: International Conference on Learning Representations Workshop.
Srinivasan, S., Righetti, R., Ophir, J., 2003. Trade-offs between the axial resolution and the signal-to-noise ratio in elastography. Ultrasound Med. Biol. 29 (6), 847–866.
Techavipoo, U., Varghese, T., 2004. Wavelet denoising of displacement estimates in elastography. Ultrasound Med. Biol. 30 (4), 477–491.
Thung, K.-H., Wee, C.-Y., 2018. A brief review on multi-task learning. Multimed. Tools Appl. 77 (22), 29705–29725.
Treece, G., Lindop, J., Chen, L., Housden, J., Prager, R., Gee, A., 2011. Real-time quasi-static ultrasound elastography. Interface Focus 1, 540–552.
Vapnik, V., Izmailov, R., 2015. Learning using privileged information: similarity control and knowledge transfer. J. Mach. Learn. Res. (16) 2023–2049.
Vapnik, V., Vashist, A., 2009. A new learning paradigm: learning using privileged information. Neural Netw. (22) 544–557.
Vapnik, V.N., 1998. Statistical Learning Theory. Wiley-Interscience.
Wainwright, M.J., Jordan, M.I., 2008. Graphical models, exponential families, and variational inference. Found. Trends Mach. Learn. 1 (1–2), 1–305.
Walker, W.F., Trahey, G.E., 1995. A fundamental limit on delay estimation using partially correlated speckle signals. IEEE Trans. Ultrason. Ferroelectr. Frequency Control 42 (2), 301–308.
Wu, S., Gao, Z., Luo, J., Liu, Z., Zhang, H., Li, S., 2018. Direct reconstruction of ultrasound elastography using an end-to-end deep neural network. In: International Conference on Medical Image Computing and Computer-Assisted Intervention (MICCAI), pp. 374–382.
Würfl, T., Ghesu, F.C., Christlein, V., Maier, A., 2016. Deep learning computed tomography. In: International Conference on Medical Image Computing and Computer-Assisted Intervention (MICCAI), pp. 432–440.
Xu, C., Xu, L., Gao, Z., Zhao, S., Zhang, H., Zhang, Y., Du, X., Zhao, S., Ghista, D., Liu, H., Li, S., 2018. Direct delineation of myocardial infarction without contrast agents using a joint motion feature learning architecture. Med. Image Anal. 50, 82–94.
Yuan, J., Zhang, H., Lu, M., Chen, S., Liu, H., 2011. A strain-based ultrasound elastography using phase shift with prior estimates and meshfree shape function. In: IEEE International Symposium on Biomedical Imaging: From Nano to Macro (ISBI), pp. 532–535.
Yuan, L., Pedersen, P.C., 2015. Analytical phase-tracking-based strain estimation for ultrasound elasticity. IEEE Trans. Ultrason. Ferroelectr. Frequency Control 62 (1), 185–207.
Zahiri-Azar, R., Salcudean, S.E., 2006. Motion estimation in ultrasound images using time domain cross correlation with prior estimates. IEEE Trans. Biomed. Eng. 53 (10), 1990–2000.
Zakaria, T., Qin, Z., Maurice, R.L., 2010. Optical-flow-based b-mode elastography: application in the hypertensive rat carotid. IEEE Trans. Med. Imaging 29 (2), 570–578.
Zaleska-Dorobisz, U., Kaczorowski, K., Pawluś, A., Puchalska, A., Inglot, M., 2014. Ultrasound elastography: review of techniques and its clinical applications. Adv. Clin. Exp. Med. 23 (4), 645–655.
Zhang, C., Bengio, S., Hardt, M., Recht, B., Vinyals, O., 2017. Understanding deep learning requires rethinking generalization. In: International Conference on Learning Representations (ICLR).
Zhang, K., Wang, Z., Zhang, J., Schölkopf, B., 2016. On estimation of functional causal models: general results and application to the post-nonlinear causal model. ACM Trans. Intell. Syst. Technol. 7 (2), 1–23.
Zhang, Y., Lv, Q., Yin, Y., Xie, M., Xiang, F., Lu, C., Yan, T., Li, W., Xu, H., Huang, Y., 2009. The value of ultrasound elastography in differential diagnosis of superficial lymph nodes. Front. Med. China 3 (3), 368–374.
Zhang, Y., Yang, Q., 2018. A survey on multi-task learning arXiv:1707.08114.
Zhao, S., Gao, Z., Zhang, H., Xie, Y., Luo, J., Ghista, D., Wei, Z., Bi, X., Xiong, H., Xu, C., Li, S., 2018. Robust segmentation of intima-media borders with different morphologies and dynamics during the cardiac cycle. IEEE J. Biomed. Health Inf. 22 (5), 1571–1582.
Zheng, X., Shi, J., Ying, S., Zhang, Q., Li, Y., 2016. Improving single-modal neuroimaging based diagnosis of brain disorders via boosted privileged information learning framework. In: MICCAI Workshop on Machine Learning in Medical Imaging (MLMI), pp. 95–103.
Zhu, Y., Hall, T.J., 2002. A modified block matching method for real-time freehand strain imaging. Ultrason. Imaging 24 (3), 161–176.